INL/JOU-23-71446-Revision-0

# Particle size and shape effect of Crumbler rotary shear-milled granular woody biomass on the performance of Acrison screw feeder: A computational and experimental investigation

Ahmed Hamed, Yidong Xia, Nepu Saha, Jordan Lee Klinger, David N. Lanning, James H. Dooley

INL/JOU-23-71446-Revision-0

# Particle size and shape effect of Crumbler rotary shear-milled granular woody biomass on the performance of Acrison screw feeder: A computational and experimental investigation

**Ahmed Hamed, Yidong Xia, Nepu Saha, Jordan Lee Klinger, David N. Lanning, James H. Dooley**

**September 2023**

**Idaho National Laboratory**
**Idaho Falls, Idaho 83415**

**http://www.inl.gov**

**Prepared for the**
**U.S. Department of Energy**
**Under DOE Idaho Operations Office**
**Contract DE-AC07-05ID14517**

# Particle size and shape effect of Crumbler® rotary shear-milled granular woody biomass on the performance of Acrison® screw feeder: A computational and experimental investigation

Ahmed Hamed[a,*], Yidong Xia[a,†], Nepu Saha[a], Jordan Klinger[a], David N. Lanning[b], James H. Dooley[b]

[a] Energy and Environmental Science & Technology Directorate, Idaho National Laboratory, Idaho Falls, ID 83415, USA
[b] Forest Concepts LLC, Auburn, WA 98001, USA

## Abstract

Physical experiments and discrete element model (DEM) simulations are conducted to evaluate particle characteristics and operation parameter effects on screw feeding performance for rotary shear-milled Douglas fir. Three performance metrics are used: mass flow rate, shaft driving torque, and specific energy consumption. The impact of particle size, particle size distribution (PSD), shaft rotational speed (rpm), and hopper dimensions on the performance are investigated. All employed performance metrics reveal the superior flowability of the 2-mm particles in contrast to the larger 6-mm counterpart. Remarkably, wider PSD results in poorer flowability than the two mono-sized particles, proving the flowability enhancement achieved by narrower PSD of the woody feedstock. More importantly, DEM simulations unveil PSD-induced degradation in flowability is attributed to mechanical interlocking and particle segregation effects. Furthermore, higher shaft rpm causes higher mass flow rate at the cost of higher specific energy consumption due to viscous dissipation and changes in flow pattern.

Keywords: Screw feeder; discrete element method (DEM); mechanical size reduction; biomass feedstocks; Douglas fir; granular flow.

---

[*] Corresponding author: Ahmed Hamed (Ahmed.Hamed@inl.gov)
[†] Co-corresponding author: Yidong Xia (Yidong.Xia@inl.gov)

# 1 Introduction

Biomass is an abundant, versatile source of renewable energy that can be used to generate power on demand and produce bio-based fuels, chemicals, and materials [1]. Advances in bioenergy research will enable this energy source to play a vital role in shaping the clean energy portfolio to meet increasing global energy demands, while satisfying the proposed measures to mitigate climate changes [2]. Harnessing the full potential of bioenergy as a strategic player in the transition to carbon-neutral energy sources is contingent upon the deployment of this technology at commercial scale becoming economically viable. To achieve this goal, efficient processes need to be developed for different unit operations along the bioenergy value chain, from harvesting the raw biomass materials all the way up to their lifetime in the biorefinery. The unique technical challenges associated with the life cycle of biomass feedstocks is mainly attributed to the undesirable characteristics of their raw form, e.g., high variability, high moisture and oxygen content, low bulk density, low calorific value, and hydrophilic nature [3–5]. Accordingly, biomass preprocessing is required to produce high-quality feedstocks using mechanical, chemical, and thermal processes that change the physical properties and chemical composition of the raw materials [6,7]. Being energy-intensive techniques, biomass preprocessing represents the highest contributor to the total cost of generating bioenergy from granular biomass feedstocks. The other substantial component in the total cost belongs to logistic operations such as materials handling, storage, transportation, and reactor feeding [8–11].

The challenges associated with materials handling and feeding are particularly ascribed to the poor flowability of the granular biomass particles. Unlike other industries involving the handling of particulate materials with favorable flow properties (including low compressibility, low cohesion, small particle size, and narrow particle size distribution), e.g., pharmaceutical, powder metallurgy, and food processing industries, the biofuel production industry typically operates under an average feeding rate much lower than a facility's design capacity. Increased downtime is the origin of this low feeding rate, which arises from materials jamming, clogging, erratic flow, particle segregation, and loss of live storage volumes because of stored materials adhering to the container walls [12–16] . Structural failure is another consequence of the flow problems-induced transient stresses during extreme circumstances. An example of the missed business opportunities is the reported biofuel production rate in 2016, which only achieved 7% of its total active rated capacity estimated at about 58 million gallons per year [15]. The unique characteristic of the lignocellulosic biomass feedstocks dictates developing dedicated design practices for handling and feeding units beyond the conventional methods that are based on decades-long accumulated experience from other industries dealing with particulate materials with substantially better flow properties. This, in turn, requires promoting an adequate understanding of the characteristic nature of the granular biomass flow behavior and the underlying transport mechanisms.

The flow behavior of particulate biomass materials is typically intermediate between solids and liquids. Individual particles and bulk biomass have complex viscoelastic deformation under stress. Under short-term low loading, the yield stress can withstand imposed stresses without any significant deformation up to a threshold value. Stresses above this threshold value causes permanent deformation in a complex fashion that involves localized elastic and plastic strains, arising from the discrete nature of the particles, and exhibits nonlinear flow response to the applied external forces. Bonn et al. [17] presented a comprehensive review of the physical origins and rheological consequences of this type of behavior. The threshold stress required for the onset of permanent deformation depends strongly upon the inter-particle friction and is very sensitive to the stress and deformation histories [15]. Difficulties associated with the handling and feeding of biomass feedstocks are not originating only from the traditional rheological properties such as bulk density, moisture content, compressibility, cohesive and adhesive strengths, as it is also affected by the chemical composition of individual particles, internal microstructure, entrapped gases, and temperature. Very recently, Navar et al. [18] studied the impact of moisture content on the rheological properties of different anatomical fractions of loblolly pine using FT4 powder rheometer. While some anatomical fractions (bark and needle) exhibited direct relation between the moisture content and the rheological properties, no influence was observed for other fractions (stem and whole). In addition, the impact of the moisture content on the rheological properties was only present for the smaller particle size of bark and needle (2 mm). The moisture content effects on the flowability for the larger particle size (4 mm) were absent for the four different anatomical fractions considered in that study. Moreover, same-size particles from different fractions showed different flowability. This demonstrates the inherent variability of the biomass feedstocks attributes and their impact on the final product quality. So, it is extremely important to thoroughly quantify the impact of different material attributes on the performance of different unit operations along the supply chain, to understand the interplay between them and assess the critical parameters. Taking conversion pathways as an example, biochemical conversion processes tolerate variations in particle shape and size, and thus the specifications of these properties are mainly constrained by other feedstock handling and flowability requirements. Contrarily, the efficiency of thermochemical conversion processes is very sensitive to the particle geometry [19,20]. Accordingly, optimizing particle characteristics for enhanced flowability is one goal in a multi-objective optimization problem that should account for other aspects across the upstream and downstream processes.

Traditionally, empirical techniques are used to optimize the performance of individual processes by seeking univariate trial-and-error methods. Alternatively, the quality-by-design (QbD) approach can be employed to systematically improve the product and process quality in a streamlined way. The concept of QbD was originally introduced by Joseph Juran [21] and used extensively in the pharmaceutical industry. It is a holistic approach applying science-based and risk-management methodologies to identify critical materials attributes (CMAs) and critical process parameters (CPPs), define critical quality attributes (CQAs), and acquire a thorough understanding of the impact of the involved materials and processes on the final product quality [22]. The analysis of the interrelations between different CMAs, CPPs, and CQAs should also determine the sensitivity of the end-product quality to any variation in the considered critical parameters. Motivated by the QbD approach, the present study integrates computational and experimental works to investigate the effect of particle characteristics of rotary sheared (Crumbles®) Douglas fir ("Df") particles on the performance of a pilot-scale handling unit – the Acrison® screw feeder system consisting of a hopper, an agitator, and a screw conveyor. Three CQAs are defined and used as benchmark metrics to quantify the flowability of the comminuted particles under different mechanical loading conditions. These CQAs are 1) mass throughput, 2) driving shaft torque, and 3) specific mechanical energy consumption. Experiments and discrete element method (DEM) simulations are conducted to evaluate the impact of one CMA (particle size) on the chosen CQAs. Df particles from veneer, milled by the Forest Concepts Crumbler® rotary shear system, are used in the current work. The studied particle sizes are in the range between 2 mm and 6 mm, as this range is of interest to several thermochemical and biochemical conversion processes. The impact of an additional CMA, i.e., particle size distribution (PSD), and two CPPs, namely, shaft rotational speed (rpm) and hopper dimension, are also investigated using DEM simulations. Moreover, the influence of the surface roughness on the DEM predictions is studied using two different particle shape models.

It is worth mentioning that the Crumbler® rotary shear addresses problems common to traditional size reduction techniques such as hammermills, grinder, and chippers. These problems typically include the production of large numbers of fines with wide PSD and poor flowability, the requirement of the energy-intensive pre-drying of the biomass particles before hammermilling, and/or the limitations on the smallest achievable particle size of about one centimeter. Crumbles from veneer material is selected because of its known satisfactory gravity-driven flow behavior with observed particle size-dependence evidenced by the authors' previous study [23]. In that study, static angle of repose (AOR), which is a good indicator of slope stability, was employed as a quantitative measure of flowability using the bottomless cylinder test [24,25]. In addition, specific energy consumption for the comminution using the Crumbler® rotary shear system was also reported [23]. Figure 1 illustrates the particle size effect on both the static AOR and comminution energy from experiment and DEM simulations. Evidently, the improved gravity-driven flowability achieved by reducing the size of the Crumbles from veneer from 6 mm to 2 mm comes at the cost of comminution energy increase by a factor of six. Anecdotal evidence from various research laboratories and scholars also give preference to the use of feedstocks from veneer to benefit from the observed good flow behavior through hoppers and screw feeders. Moreover, the characteristic features of veneer particles are believed to help precise reactor tuning. These features include the high surface checking and the uniform particle length.

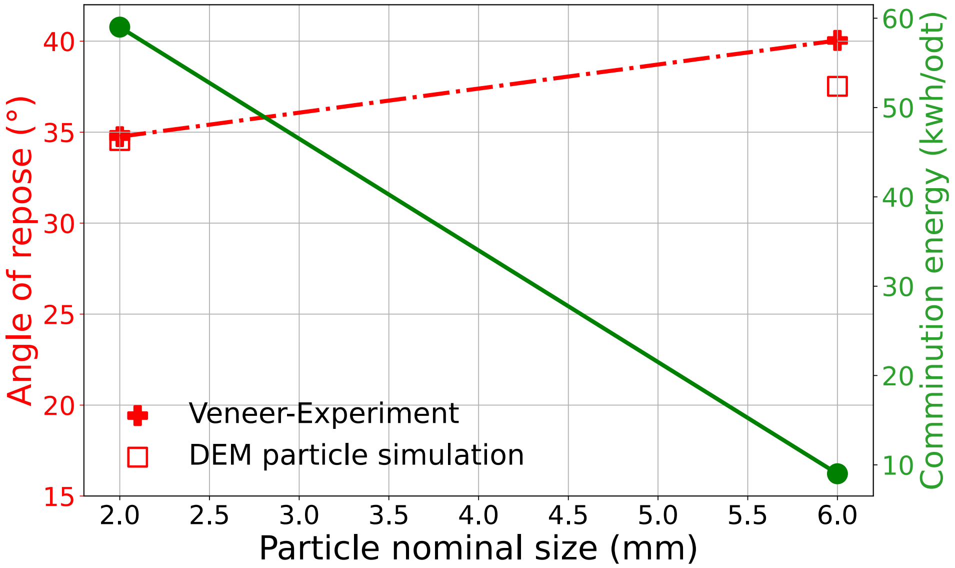

Figure 1. Impact of particle size on the static AOR for crumbles from Veneer using experiment and simulation (left axis) along with the measured energy of comminution using the Forest Concepts Crumbler® rotary shear system in units of kilowatt-hour per oven-dry ton (right axis).

Under dynamic loading conditions, the granular flow behavior can be classified into three different regimes, namely, 1) quasi-static shearing, 2) inertial, and 3) intermediate transitional flows [26,27]. While the quasi-static shearing flow regime represents one extreme that occurs in dense and confined granular assemblies [28,29], the inertial flow is the opposite extreme that is typically encountered in the dilute limit where the granular particles are loose and interacting mainly through uncorrelated binary collisions [30,31]. Theoretical formulation of elastoplastic solids and the kinetic theory of dense gases can be adequately applied to the two different regimes, respectively. On the other hand, the intermediate transitional flow regime is so far still poorly understood. Thus, numerical experiments are needed to complement theoretical prediction and aid in bridging the gap between the microscopic properties and the macroscopic behavior of granular materials.

DEM is an adept framework to capture the emergent dynamics due to the discrete nature of the granular particles and resolve the interplay between the underlying mechanisms including the attractive (or cohesive) forces exerted by the intermolecular interactions (e.g., Van der Waals bonding and capillary forces) and repulsive/dissipative forces such as interparticle contact friction and rolling resistance. For example, Chen et al. [32,33] used DEM simulations to elucidate the importance of accounting for particle morphology for a reliable prediction of flow behavior of coarse aggregate of ballast materials, as interlocking effects becomes prevalent. On the other hand, the mechanical response of fine particles was mainly determined by particle size. In addition to particle size, sliding and rolling frictions were demonstrated to be the predominant factors in the determination of the AOR of sandpile. Contrarily, other mechanical properties such as Young's modulus, Poisson's ratio, bulk density, and damping coefficients had minimal effects [34].

The significant increase of computing power and accessibility to superior computational resources availed the use of DEM in simulating real feeding systems of granular materials such as screw conveyors [35]. For example, Kretz et al. [36] demonstrated the application of DEM in screw feeding simulations and its capability to reproduce the experimental results. The flow behavior of cohesive particles in a screw feeder at three different regimes, namely, continuous, intermittent, and stable arch flow was studied by Hou et al. [37] using DEM. Moreover, Wang et al. [38] employed DEM simulations of screw conveyor to explore the particle flow behavior and transport processes at different screw rotating speeds. Furthermore, DEM was utilized to optimize the geometry of screw conveyors for premixing actions during bulk materials transport by Pezo et al. [39]. Spherical granules made from zeolite with different colors were used in that study as the representative bulk materials. A recent literature review of the reported granular flow behavior in screw feeders and conveyors was conducted by Minglani et al. [40]. Nevertheless, special attention needs to be paid when applying DEM to study the transport of biomass materials due to its high variability and lack of standardized methods to accurately characterize particle features. Rackl et al. [41] reported their experimentally observed influence of different grades of wood chips on the performance of a screw feeding systems. Likewise, Falk et al. [42] investigated experimentally the screw feeding performance of a range of biomass materials milled using two different methods, namely, cutting mill and hammermill. Using principal component analysis, the authors found long-time correlations between feeding variability (fed at constant rpm) and AOR. Moreover, short-time correlations with Hausner and compression ratios were also observed.

Given the serious problems that are commonly encountered during the handling of granular biomass materials at the industrial scale leading to lack of flow or extended downtimes, more knowledge needs to be gained about the granular flow behavior of this intricate type of materials and emergent phenomena. In this regard, the present communication elucidates the relation between the particle characteristics of Crumbler® milled biomass feedstocks and their transport behavior with emphasis on the impact of the uniform shape and narrow particle size distribution characterizing the Crumbles materials on the performance of screw feeding system. The goal is twofold: The first is concerned with promoting better understanding of underlying mechanisms by quantitatively assess the role played by CMAs, which can aid in optimal selection of mechanical preprocessing requirements; the second objective is to shed light on the impact of common practices in the DEM simulations of biomass materials on the model predictability.

The rest of the paper is organized as follows: In the next section, the preparation of the Crumbles from veneer samples and the Acrison test of the Crumbles flowability and measurements are described. In addition, the computational approach is detailed in the same section. In section **3**, the DEM simulation results of the considered CQAs are presented and compared with the experimental results. Moreover, the implications of different CMAs (e.g., particle size and PSD) and CPP (the screw shaft rpm) to the performance of the screw feeder system, in terms of the selected benchmark metrics, are discussed. Furthermore, the computational cost of the DEM simulations is analyzed. Finally, the summary, key findings, and conclusive remarks are outlined in section **4** along with an outlook for future research.

## 2 Materials and Methods

## 2.1 Crumbles from Veneer

As noted earlier, comminution is a key preprocessing step for feedstocks. Comminution method has a strong impact on the feeding behavior, see for example [43]. Several mechanical size reduction techniques applying either impact, shear, or compression forces are usually used to produce biomass feedstocks with different qualities. For example, using the same screen size, hammermills (which are widely used in high-throughput industrial-scale applications) tends to produce more fine particle sizes and wider PSD than knife mills, which are typically used for laboratory sample preparation [15]. The targeted particle size depends on the biofuel conversion application. Whereas a nominal (geometric mean) particle size of 6 mm is common for gasification, a nominal particle size specification of 2 mm is often used for catalytic fast pyrolysis. Based on the pretreatment process, both sizes can be used for biochemical conversion and lie within the typical range for thermal conversion of forestry residue-derived biomass. Wide PSD can lead to different set of problems. For example, fine particles reduce the permeability of bulk solids to gas and liquids. On the other hand, over-sized particles cause incomplete conversion, feeding system jams, and air locks plugging. Thus, deviations in particle size specifications have direct impact on the feeding and conversion performance. The Forest Concepts Crumbler® rotary shear milling and screening system efficiently produces evenly shaped particles with less fines, narrow PSD, and high flowability. In addition, biomass with any moisture content can be processed without pre-drying.

For the present study, a set of “matched” bulk feedstock samples from conifer veneer were produced by Forest Concepts, LLC. The veneer was made from freshly cut Douglas fir logs using a centerless veneer lathe. In March 2021, Forest Concepts received the sectioned logs of a single Douglas fir tree that was locally harvested in Edgewood, WA. Two logs were used in the processing of the wood veneer with short sections assigned alternately between them. In addition, separate lathe settings were applied during the processing of the log lots to produce the 2mm and 6mm nominal thicknesses required for the downstream processing. The final comminuted feedstock samples were produced at two different nominal particle sizes of 2 mm and 6 mm using the Crumbler® rotary shear milling and screening system, specifically, Forest Concepts Model M24S-30e rotary shear milling system and Model 2448 orbital screen system. Because the particle thickness was controlled by the veneer process and the particle length was controlled by orientation of the veneer sheet into the rotary shear, the produced Crumbles from veneer had a uniform cubic shape [44]. Milled particles were dried for a period of 12–16 hours in custom cabinet-type downdraft dryer by Forest Concepts, with temperature set for 40–50 $^{\circ}$C. Low temperature drying is used to preclude loos of volatile organic compounds and avoid any thermally induced modification of the bulk material. The feedstocks were dried to less than 10 percent wet-weight basis (%wb), while the initial moisture content of the raw Douglas fir wood veneer was in the typical range for green wood (37–44 %wb). The as-shipped samples had bulk density of 124–151 kg/m$^3$. The porosity analysis of X-ray Computed Tomography (CT) scanning images of different batches showed similar microstructure and porosity between the 2-mm and 6-mm particles [45]. The retained native microstructure suppresses the expected increase in transport resistance in the case of larger particle size. Hence, this comminution method can help relax the small particle size requirements in thermochemical conversion processes, which is dictated by the conversion efficiency. In addition, it aids the scope of the present study by singling out particle size effects without interference with microstructure effects.

## 2.2 The Acrison® Test and Flowability Measurements

The feeding behavior of each sample was tested using the Acrison® Bin Weight Screw Feeder (model 402X-250-75-BDF1.5-E/2). The unit consists of a large feed bin atop an interchangeable feed screw auger and two mixing augers slightly above the feed screw to mix the material and ensure reliable flow from the bin into the screw. The entire unit is mounted on a load cell to measure the system mass, allowing for measurements of the feed rate. These tests were conducted using a 63 mm diameter solid shaft screw with two different discharge mechanisms. Figure 2 shows batches of the tested samples and the experimental setups. To benchmark the computed shaft torque from DEM simulation results against the experimentally measured torque, a region of interest (ROI) was selected that accounts only for the torque acting on the external part of the screw feeder, which is not affected by the action of the two mixing augers or feed material weight inside the large feed bin. Accordingly, each sample was tested using two different setups. In the original setup, the material travels through an extended conduit for 250 mm before being discharged into the discharge bin. In contrast, for the modified setup, the material is discharged right after the feed bin and thus bypass the ROI. A FUTEK torque sensor (model USB250) was connected to the auger to record the torque in the auger during the test. The sensor was installed in between the motor and the auger as shown in Figure SA in the supplementary material. During a typical test, the unit was operated at a constant shaft rotational velocity of 48 rpm. For each test, the unit was set to operate for an initial period of 2 minutes without any sample in the feed bin to establish the average baseline torque. About 25 kg of the material was then introduced into the feeding bin, and the unit was allowed to operate until the mass flow rate reached a very low value (i.e., less than 5 kg/h). For all tests, the mass feed rate and torque in the auger were recorded by the feeder controller and torque sensor, respectively at a 5 Hz frequency. To ensure synchronization of the mass and torque measurements, the time scales of these devices were aligned with each other using the recorded digital timestamp. These data were further used to validate the model. It is important to note that the readability of the weight balance used was within ±10 g, while the torque sensor was within ±0.001 N·m. The weight balance was calibrated annually, and at the time of the experiments showed an error of less than 0.1 % error with calibration weights. The torque sensor was calibrated prior to the experiment with a digital torque wrench with tracible certification. The calibration curve for the torque sensor is shown in supplementary information Figure SB. The average calibration accuracy of the torque sensor was ±0.29 N·m (< 0.3%) over the full range of 200 N·m. This calibration curve showed that the sensor reading linearly followed the applied torque. However, the sensor reading was consistently higher than the applied torque. Therefore, the experimental torque values were adjusted by the calibration factor.

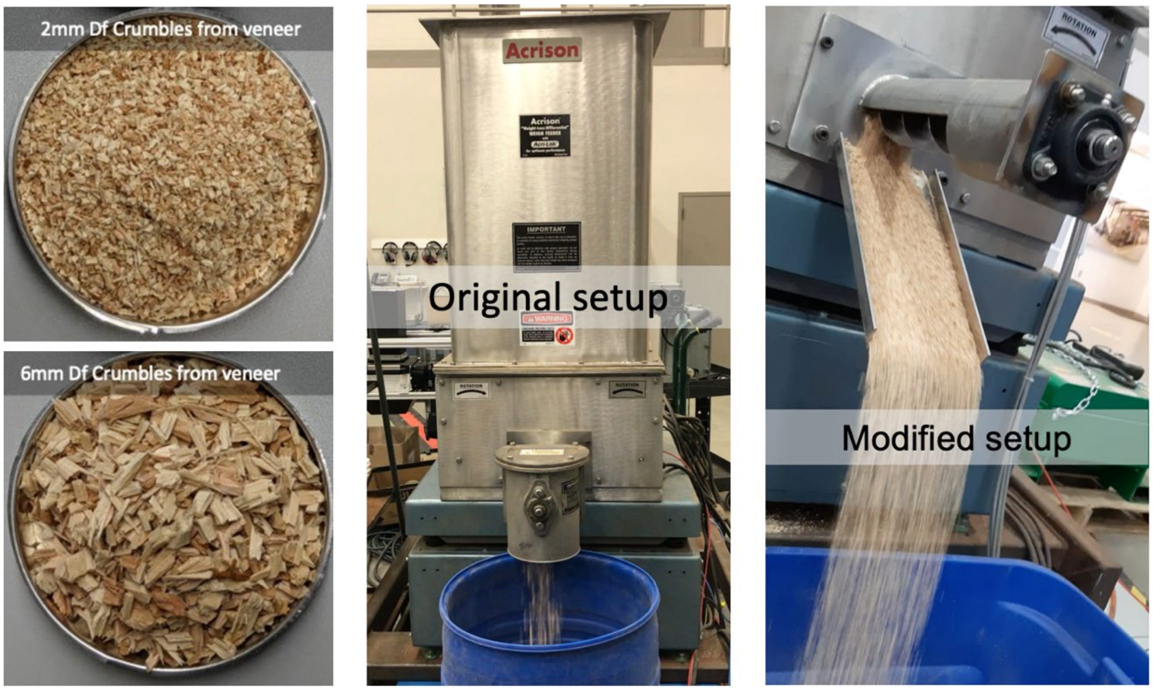

Figure 2. Experimental setup and the Acrison screw feeder system at Idaho National Laboratory: Samples of the two different sizes of Crumbler comminuted Douglas fir pine particle from veneer (left), the original setup of the Acrison system (middle), and the modified Acrison system setup allowing Veneer particles to bypass the external part of the screw shaft (right).

Figures 3(a) and 3(b) show the measured temporal profile of the mass discharge rate from the original and the modified setups for the 2-mm and 6-mm particle sizes of Df Crumbles, respectively. For the 2-mm particle size case, the test using the original setup was conducted twice to examine the initial packing effects on the measurements, which turned out to be negligible. So, no duplicate tests were repeated for the rest of the cases. Over the course of each test, the observed mass flow rate was approximately constant. In this regard, it is worth mentioning that the spikes near the end of measurements of the mass discharge rate in Figures 3(a) and 3(b) are attributed to the manual flattening of the discharged material heap to fit into the collection bucket and are discarded in the further analysis of the mass throughput to be shown later. Similarly, the measured total torque temporal profile for the 2-mm and 6-mm particles are plotted in Figures 3(c) and 3(d), respectively. In addition, the torque acting on the ROI (shaft torque) is calculated by subtracting the measured total torque for the modified setup test from the total torque in the original setup test. The obtained temporal profiles are displayed in Figures 3(e) and 3(f). Although the total torques exhibit a diminishing behavior versus time, the fluctuations in the shaft torque profiles are more pronounced and continue to the end of the test. It is noteworthy that the mass flowrate remained relatively constant during the experiment, while the total torque decreased gradually over time. The feeder was operated in a constant discharge mode, thereby sustaining a steady mass flowrate throughout the duration of the experiment. However, the reduction in torque could be attributed to the decrease in material loading height over time, as the material continued to discharge from the feed bin.

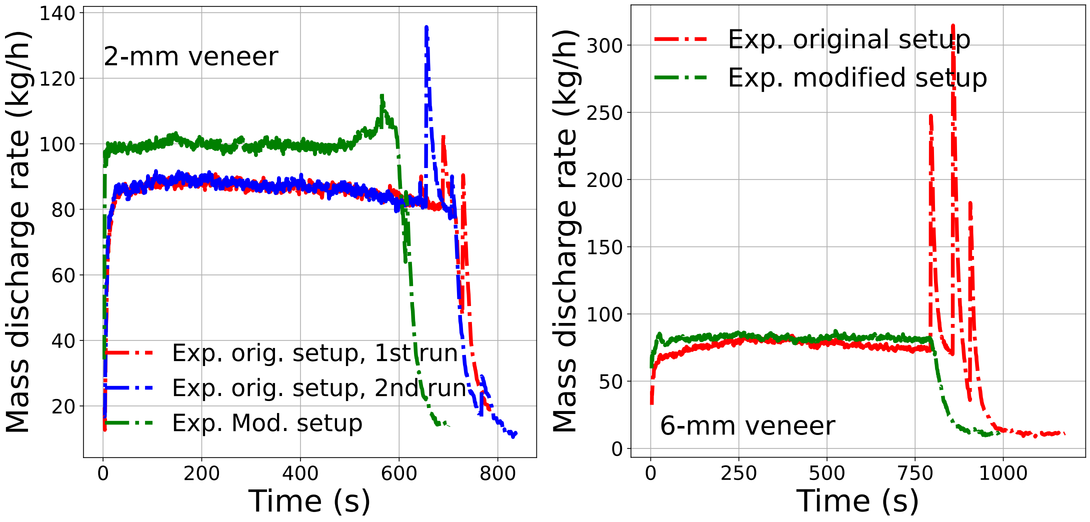

(a) (b)

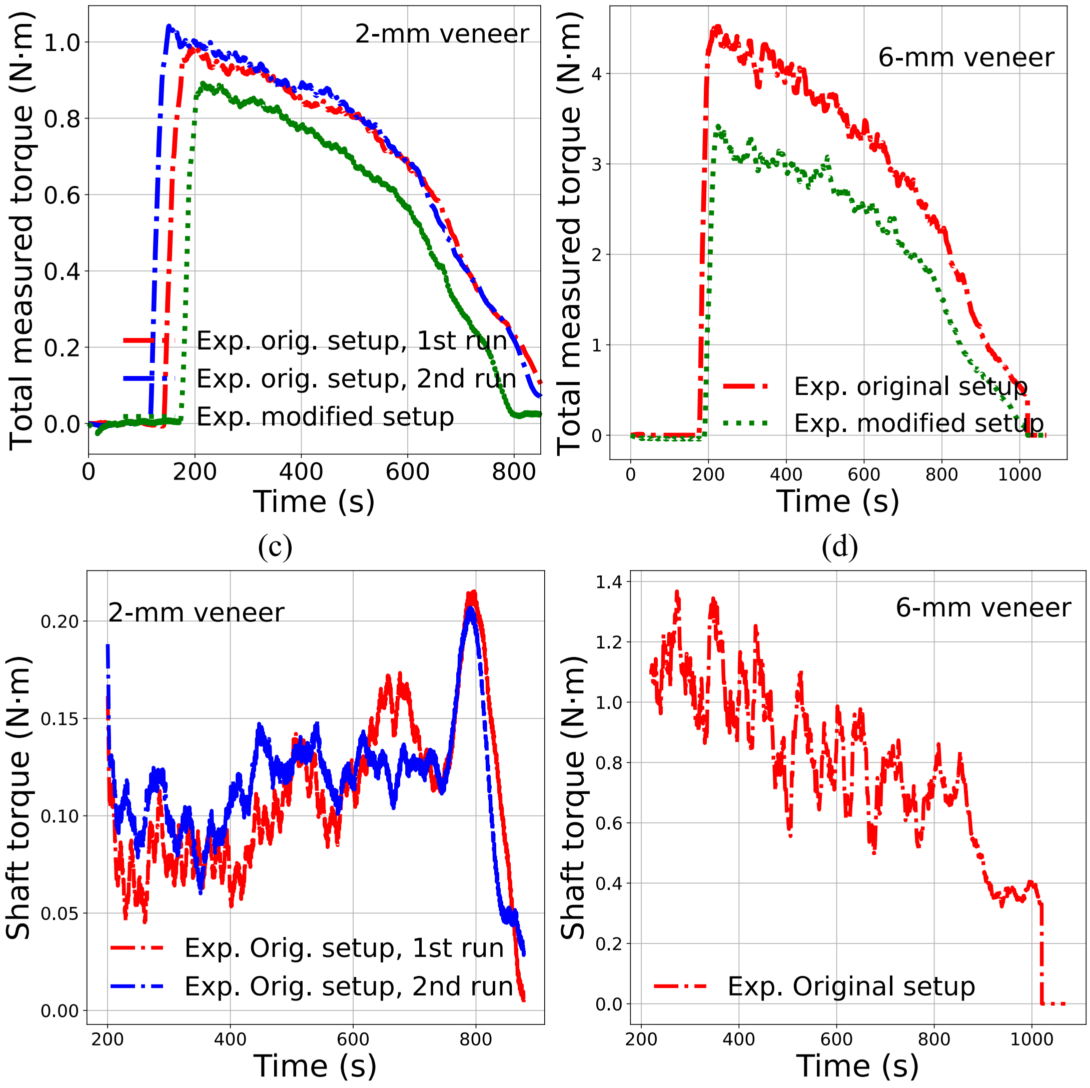

(c) (d)

(e) (f)

Figure 3. Mass discharge rate versus time for the Acrison system test of the 2-mm (a) and 6-mm (b) Crumbles from veneer using the original and the modified experimental setups at a shaft rotational speed of 48 rpm. (c) and (d) The corresponding total torque versus time measured for the same cases in (a) and (b), respectively. (e) and (f) The evaluated torque acting on the external part of the screw feeder (ROI) versus time for the 2-mm and 6-mm veneer, respectively.

## 2.3 Computational Approach

### 2.3.1 DEM Model Description

DEM approach comprises a family of computational algorithms that use particle-based description to simulate materials behavior and track individual constituents' evolution in phase space using Newton's equation of motion. DEM is widely used to tackle the dynamics of particulate systems in fields such as rock mechanics, powder mechanics, and granular flow [10,46–48]. Originally introduced by Cundall and Strack [49], DEM employs a theoretical framework like molecular dynamics (MD) without resolving the atomic structure. As such, a single DEM particle is a coarse-grained representation of material ensemble with a finite size spanning various length scales typically starting from sub-micrometer up to a few centimeters. In addition, rotational degrees of freedom are explicitly accounted for as well as stateful contact. Although DEM particle can by design feature geometries that capture the high-resolution granular particle morphology, this is in many cases computationally prohibitive. Accordingly, the common practice is to use simple shapes for this purpose, with single sphere being the most widely used shape to model the DEM particle. This preference of single sphere shape is because of the remarkable reduction in the computational cost gained from cheaper force calculations and simpler contact detection algorithms. Efficient scaling on parallel computers is another motivation to adopt simple shape particle models. Real particle shape effects on the simulated material response are effectively captured via the use of a rolling resistance model with the coefficient of rolling friction being an adjustable parameter that can be tuned to reproduce the experimentally observed dynamics [50,51]. Nonetheless, the predictability of this practice is open to question, as model parameter recalibration is usually required for different loading conditions. Clumped-sphere particle shape model is a better resolved approximation of complex-shaped particles [52]. Each clumped-sphere particle is formed by spatially arranging several rigid base spheres in a pattern resembling the targeted shape with unbreakable bonds connecting them. Consequently, clumped-sphere models can capture particle morphology and surface roughness and admit more realistic simulation of interparticle deformation. However, they have limited applicability in scenarios where intraparticle deformation and/or breakage are important, e.g., the simulation of comminution processes. For such scenarios, the bonded-sphere models [53–55] are better suited. In this class of models, the deformable nature of the bonds connecting the base-spheres comprising individual DEM particle allow relative displacements in response to external forces. Moreover, these bonds are assigned maximum strength and can undergo breakage according to a predefined criterion based on the normal or shear stress state. New bonds can also be created. The tracking of the additional degrees of freedom associated with the bonds connecting the base spheres makes this class of models more computationally intensive. For more information about bonded-sphere models, reader can refer for example to [56]. In addition, Xia et al. [11] have recently reviewed the cutting-edge DEM models for simulating the flow of milled granular biomass.

The scope of the current study focuses on the flow behavior in screw conveyor within the intermediate range of shaft rpm belonging to the linear regime of the conveyor volumetric throughput. This corresponds to relatively small values of Froude number, which measures the ratio between the centrifugal and inertial forces, far from the cataracting (mainly used in milling processes) and centrifuging granular flow regimes [57–59]. So, deformation of individual granular particles is expected to have a minimal impact on the overall dynamics. Accordingly, clumped-sphere class was chosen here as the DEM particle model to account for particle shape and capture surface roughness-induced mechanical interlocking while restraining the computational cost and total simulation time.

### 2.3.2 Fundamental Model Formulation

Conservation of linear and angular momentums are the fundamental equations governing system evolution in DEM simulations. Accordingly, for a particle $i$, its translational and rotational motions are given by, respectively,

$$m_i \ddot{\mathbf{r}}_i = \sum_{j=1}^{N} \mathbf{F}_{ij} + m_i \mathbf{g}; \tag{1}$$

$$I_i \dot{\boldsymbol{\omega}}_i = \sum_{j=1}^{N} \mathbf{M}_{ij}. \tag{2}$$

The subscripts in these equations label the particle index; $m$ is the particle mass; $\mathbf{r}$ and $\boldsymbol{\omega}$ denotes the position vector and rotational velocity, respectively; $\mathbf{F}$ and $\mathbf{M}$ designate the pairwise interaction force and torque, respectively, exerted by particle $j$ on particle $i$; and $\mathbf{g}$ is gravity. In this convention, it should be born in mind that particle self-interaction is excluded, i.e., $i \neq j$. In addition, $N$ refers to the total number of particles in the system. Unless otherwise stated, the Hertz-Mindlin contact model [60,61] is used in the current work to represent the particle-particle interaction forces. Within this formulation, the contact forces consist of two resolved components corresponding to the normal and tangential forces. The normal force is given by an additive composition of two terms representing elastic and damping forces. Likewise, the tangential force has two terms representing the elastic and damping forces. However, the nature of the tangential elastic force is different from the normal elastic force, as it corresponds to shear forces. Accordingly, the tangential elastic force is history dependent and calculated in terms of the cumulative tangential displacement between the interacting particles relative to the initial time when they are in contact with each other. In contrast, the normal elastic force takes the form of a spring force that bears no memory and directly depends on the instantaneous overlap between the particles in the normal direction. As such, the overall expression for the pairwise contact force in Hertz-Mindlin model is formulated as [54]

$$\mathbf{F}_{ij} = \mathbf{F}_{ij,n} + \mathbf{F}_{ij,t} = \left(k_n \boldsymbol{\delta}_{ij,n} - \gamma_n \mathbf{v}_{ij,n}\right) + \left(k_t \boldsymbol{\delta}_{ij,t} - \gamma_t \mathbf{v}_{ij,t}\right). \tag{3}$$

In the above, Coulomb friction limit is imposed as a constraint on the maximum magnitude of the tangential force. This yield [54]

$$\left|\mathbf{F}_{ij,t}\right| \leq f_p \left|\mathbf{F}_{ij,n}\right|; \tag{4}$$

where $k_n$ and $k_t$ stand for the elastic constants for the normal and tangential contacts; $\boldsymbol{\delta}_{ij,n}$ denotes the overlaps between the two particles in the normal direction; $\boldsymbol{\delta}_{ij,t}$ indicates the cumulative relative displacement in tangential direction from the time the two particles become in contact; $\mathbf{v}_{ij,n}$ and $\mathbf{v}_{ij,t}$ represent the relative normal and tangential velocities between the two particles at the point of contact; and $\gamma_n$ and $\gamma_t$ label the viscoelastic damping constants for the normal and tangential contacts. Moreover, $\mathbf{F}_{ij,n}$ and $\mathbf{F}_{ij,t}$ correspond to the normal and tangential contact forces, respectively; and $f_p$ is the particle friction coefficient.

The following relations are used to compute the model parameters $k_n$, $k_t$, $\boldsymbol{\delta}_{ij,n}$, and $\boldsymbol{\delta}_{ij,t}$ as functions of the material properties [54]

$$k_n = \frac{4}{3}\hat{E}\left(\hat{R}\delta_{ij,n}\right)^{1/2}; \tag{5}$$

$$k_t = 8\hat{G}\left(\hat{R}\delta_{ij,n}\right)^{1/2}; \tag{6}$$

$$\gamma_n = -2\sqrt{\frac{5}{3}}\beta\left(\hat{m}\hat{E}\right)^{1/2}\left(\hat{R}\delta_{ij,n}\right)^{1/4}; \tag{7}$$

$$\gamma_t = -4\sqrt{\frac{5}{3}}\beta\left(\hat{m}\hat{G}\right)^{1/2}\left(\hat{R}\delta_{ij,n}\right)^{1/4}. \tag{8}$$

In these relations, the equivalent Young's modulus ($\hat{E}$), radius ($\hat{R}$), shear modulus ($\hat{G}$), mass of two contacting spheres ($\hat{m}$); and the restitutions coefficients ($\beta$) take the form [54]:

$$\frac{1}{\hat{E}} = \frac{1-\nu_i^2}{E_i} + \frac{1-\nu_j^2}{E_j}; \tag{9}$$

$$\frac{1}{\hat{R}} = \frac{1}{R_i} + \frac{1}{R_j}; \tag{10}$$

$$\frac{1}{\hat{G}} = \frac{2(2-\nu_i)(1+\nu_i)}{E_i} + \frac{2(2-\nu_j)(1+\nu_j)}{E_j}; \tag{11}$$

$$\frac{1}{\hat{m}} = \frac{1}{m_i} + \frac{1}{m_j}; \tag{12}$$

$$\beta = \frac{ln(e)}{\sqrt{ln^2(e)+\pi^2}}; \qquad (13)$$

where $\nu$ labels Poisson's ratio; $E$ designates Young's modulus; $R$ and $m$ stand for the particle radius and mass, respectively; $e$ denotes the coefficient of the restitution; and again, the subscripts $i$ and $j$ correspond to the particle index.

The torque exerted by particle $j$ on particle $i$ is given by [62]

$$\mathbf{M}_{ij} = \mathbf{M}_{ij,t} + \mathbf{M}_{ij,r} + \mathbf{M}_{ij,n}. \qquad (14)$$

In the above equation, the total torque is additively decomposed into three components originating from the tangential contact forces, the rolling friction, and the normal contact forces, respectively. The last term appears in the scenario when the particle center does not lie on the normal force line of action. In addition, asymmetric normal forces give rise to rolling friction torque acting to slow down the relative rotation between the two particles. Other physical mechanisms can similarly lead to the presence of a rolling friction at the contact between two particles or a surface and particle, e.g., viscous hysteresis, surface adhesion, plastic deformation, micro-slip, and friction [62]. As noted earlier, rolling friction can also be invoked to effectively imitate the effect of real particle shape when idealized particle shapes are used. In the present work, a directional constant torque model is employed for the rolling friction. It is defined as [62]

$$\mathbf{M}_{ij,r} = -\frac{\boldsymbol{\omega}_i - \boldsymbol{\omega}_j}{|\boldsymbol{\omega}_i - \boldsymbol{\omega}_j|} \mu_r \hat{R} \left|\mathbf{F}_{ij,n}\right|; \qquad (15)$$

with $\mu_r$ being the coefficient of the rolling friction. The pairwise torque in this model always acts in the opposite direction of the relative rotation between the two interacting particles and has a magnitude that scales linearly with the pairwise normal contact force magnitude.

## 3 DEM Simulation Results & Discussion

### 3.1 Simulation Setup

As was highlighted earlier, a clumped-sphere model resembling cubic shape is used to model the Crumbles from veneer particles. Each cubic particle is composed of 8 identical base-spheres with a diameter equivalent to half of the cube side length (D). The non-overlapping base-spheres are arranged in a layout like the simple cube crystal structure, i.e., touching each other along the cube sides. Two particle sizes are considered corresponding to two cubes with side lengths, D, of 2 mm and 6 mm. In addition to the clumped-sphere model, a single sphere particle shape model was invoked for the sake of investigating particle shape effects on the model prediction. Only single spheres with a diameter of 6 mm are considered. Figure 4 illustrates the template for the two particle shape models along with the 3-D digital replica of the selected ROI of the Acrison system and the dimensions of the two used conical hoppers. The external cylindrical tube casing the screw shaft has a diameter of 63.5 mm (2.5 inch). In addition, the inlet (connected to a hopper) and outlet openings of the tubular casing have circular cross section of the same 2.5-inch diameter. The pitch and the shaft (core) diameter of the screw are 63.5 mm (2.5 inch) and 31.75 mm (1.25 inch), respectively. A small clearance exists between the external blades of the screw shaft and the casing tube meaning that the screw flighting diameter is slightly smaller than the casing tube diameter. This allows frictionless rotation of the screw shaft in the absence of particles and denies particle flow through the gap. The two conical shaped hoppers used in the current work have the same opening widths for the circular inlet and outlet (connected to the casing tube) openings with diameters of 0.25 m and 0.0635 m (2.5 inch), respectively. However, the two hoppers differ in height (0.5 m and 0.25 m) and their semi-inclination angle (76° and 63°, measured between the hopper wall and the vertical axis). It is worth noting that the capacities of these two hoppers are smaller than the actual capacity of the bin attached to the Acrison feeder system. This was necessary to render the simulations computationally affordable without affecting the comparability between the simulation and experimental results. Unless otherwise stated, the tall hopper was used in the simulations.

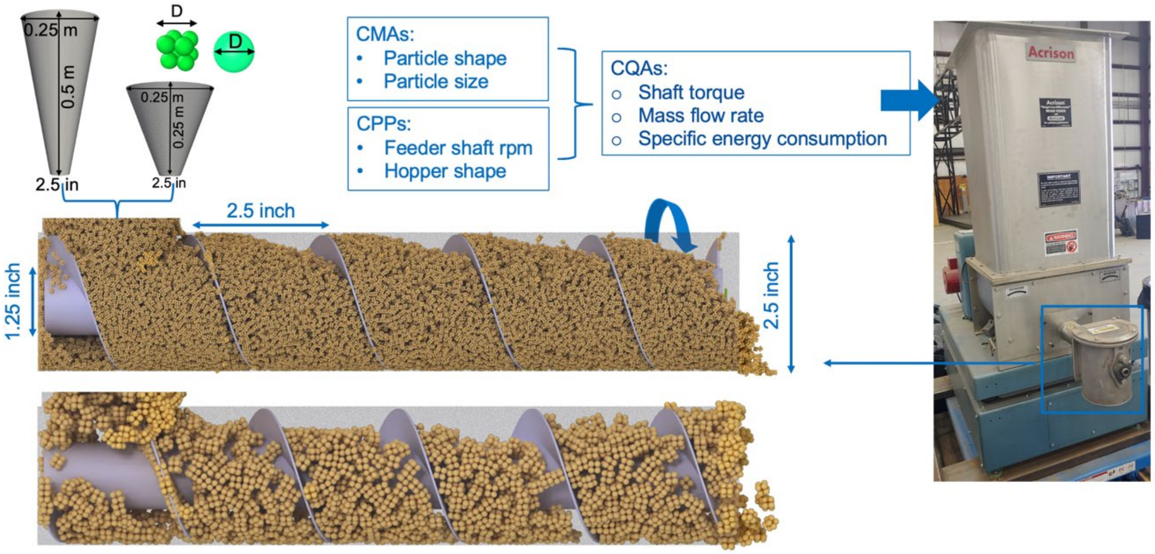

Figure 4. DEM simulation setup of the selected region of interest (ROI) of the Acrison system: Dimensions of the two conical hoppers used in the DEM screw feeder simulations along with the two consider DEM particle shapes of size D, i.e., single sphere and clumped sphere with cubic shape (top left), the dimensions of the screw shaft while filled with 2-mm clumped-sphere particles (middle left), a snapshot of DEM simulation of the 6-mm clumped-sphere particles (bottom left), a schematic diagram showing the CMAs, CPPs and CQAs considered in the present study (top middle), and the selected ROI from the Acrison system (right). DEM simulations snapshots are visualized using OVITO [63].

The digital model consisting of the hopper, screw shaft, and casing tube is discretized using triangle meshes with the screw shaft mesh having the highest resolution. During the initialization of the DEM simulations, the whole hopper was filled by DEM particles of specific shape and size using a random packing algorithm. The packing volume fraction was set to a targeted value of 0.6. This packing stage was followed by a one-second-long equilibration step, where the hopper outlet opening was kept close (resting on an impenetrable horizontal base), and the screw shaft remained stationary. Accordingly, gravity was the only acting external force during the equilibration stage. After particles rearrangement-induced transients, the system becomes completely relaxed since all particles come to rest. Afterwards, the screw feeding simulation starts by removing the impenetrable base closing the hopper outlet opening and rotating the screw shaft at a constant rpm. The considered range for the screw shaft rotational velocity was between 24 and 240 rpm. Simulations continued until all the particles are discharged from the casing tube outlet. One microsecond was used in all simulations as the timestep size. All DEM model parameters are taken from [23] and listed in Table 1. They were tuned to reproduce the experimentally measured AOR of Douglas fir material and selected from the range of parameters reported in [64], which are calibrated by compressibility test to reasonably replicate the experimentally observed frictional behavior of milled pines in a shear test. The DEM simulations were performed using LIGGHTS-INL [65,66]. This software is a capability extension of LIGGGHTS (LAMMPS improved for General Granular and Granular Heat Transfer Simulation), which is an open-source DEM particle simulation software [67]. LIGGGHTS-INL has efficient parallel computing capabilities on high-performance computer (HPC), which is very necessary for this type of computationally intensive simulations. Table 2 summarizes the different type of simulations that were performed.

Table 1. Material and contact model parameters used in DEM particle simulations [23].

| **Parameter** | **Value (default)** |
|---|---|
| **Particle density, $\boldsymbol{\rho_P}$ [kg/m$^3$]** | 300 |
| **Particle Young's modulus, $\boldsymbol{E_P}$ [Pa]** | 1×10$^6$ |
| **Particle Poisson's ratio, $\boldsymbol{\nu_P}$** | 0.3 |
| **Boundary density, $\boldsymbol{\rho_B}$ [kg/m$^3$]** | 7850 |
| **Boundary Young's modulus, $\boldsymbol{E_B}$ [Pa]** | 1×10$^{11}$ |
| **Boundary Poisson's ratio, $\boldsymbol{\nu_B}$** | 0.3 |
| **Rolling friction coefficient, $\boldsymbol{\mu_r}$** | 0.5 |
| **Particle-particle friction coefficient, $\boldsymbol{f_{P-P}}$** | 0.7 |
| **Particle-boundary friction coefficient, $\boldsymbol{f_{P-B}}$** | 0.3 |
| **Particle-particle restitution coefficient, $\boldsymbol{\beta_{P-P}}$** | 0.3 |
| **Particle-boundary restitution coefficient, $\boldsymbol{\beta_{P-B}}$** | 0.3 |

Table 2. Summary of simulated cases.

| **DEM particle** | | **Hopper height** | **Contact model** | **Shaft speeds (rpm)** |
|---|---|---|---|---|
| **Shape** | **Size** | | | |
| Clumped-sphere | 2-mm | Tall hopper | Hertz-Mindlin | [24, 48, 60] |
| | 6-mm | | | [24, 48, 60, 120, 240] |
| | Bidisperse (2- and 6-mm with equal number fraction) | | | |
| Single sphere | 6-mm | | | |
| | | | Nonlinear hysteretic | |
| | | Short hopper | | |

## 3.2 Effects of the Screw Shaft RPM on Flow Behavior and Underlying Mechanisms

The current DEM simulations make no use of any agitators in the hopper. As such, particles movement in this region of the computational domain is driven by gravity. Additionally, particle flow dynamics is affected by reaction forces due to particle-particle and particle-wall interactions. In contrast, once the particles get into the screw conveyor, they also experience the influence of the centrifugal forces originating from the rotating screw shaft with a magnitude that is proportional to the angular velocity squared. The conveying action is driven by the helical screw blades pushing the particles to move in spiral paths along the shaft axis. The friction forces between the particles and surface of the screw blades as well as the internal viscous frictions give rise to the particle vortex motion, which can decrease the transportation efficiency (the conveying action). Particle vortex motion tends to decrease (up to a limiting value) as the screw rotating velocity increases [68]. Roberts [68] developed a theoretical model to predict the volumetric performance of screw conveyor of a given geometry. The derived expression for the volumetric throughput depends on the screw conveyor geometry, its rotating velocity, and the particle packing fraction inside the screw feeder region (the filling fraction). The maximum theoretical volumetric throughput depends on the screw volumetric capacity and changes linearly with the shaft rotational velocity. However, the actual volumetric throughput shows sublinear relation with the shaft rotational velocity. This is partly because of the gravity-driven particle inflow rate at the conveyor intake becoming the rate limiting factor at high shaft rotating speed, as it results in low screw filling fraction. Moreover, as was demonstrated by Moysey and Thompson [69], increasing the shaft rotational speed above certain value leads to screw starvation phenomenon, where the channel filling fraction and particle coordination number decrease by increasing the shaft rotational speed. In addition to the screw conveyor geometry and shaft rpm, material attributes and wall friction have direct impact on the screw filling fraction and the degree of the particle vortex motion. Performance of screw conveyor in the handling of the agricultural grains was reviewed by Zareiforoush et al. [70] by mainly surveying experimental work from the literature. Theoretical models for the evaluation of screw conveyor performance employ simplifying assumptions and mainly focus on the screw design parameters, inclination angle, and operation parameters. But they lack accountability for material attributes such as particle characteristics (e.g., size and shape), particle-particle interactions, and particle-wall friction. On the other hand, most of numerical studies considered DEM simulations with spherical particles [40].

Figures 5(a) and 5(b) show the time series of the mass discharge rate and shaft torque, respectively, obtained from DEM simulations of the 6-mm clumped-sphere particle shape model (corresponding to the 6-mm Crumbles from veneer) using the shaft rotational speed employed in the experiment (48 rpm) along with the results for additional shaft rotational speeds (24, 60, 120, and 240 rpm). Although the Acrison feeder system used in the experiment has a rated shaft rotational speed of 60 rpm, higher speeds were also considered in the simulations to investigate any deviation in the mass flow rate from the linear regime, which is typically expected at high-rpm values, and to better analyze the impact of shaft rpm on the shaft torque. The plots of the mass discharge rate temporal profiles for different values of rpm in Figure 5(a) exhibit continuous flow pattern with small fluctuation about an average value and a consistent increase in this average value with the increase in the shaft rotational speed. Contrarily, the torque temporal profiles in Figure 5(b) have more pronounced oscillations that will be analyzed in Section 3.4 and follow a more complex behavior in response to the input shaft rpm. Similar trends were observed for the other DEM simulation cases. Consequently, to facilitate direct comparison with experiment and further analysis of the CPP and CMAs effects on the CQAs, time-averaging technique is employed. As will be shown later, the correlation between the shaft rpm and the mass flow rate is always positive, which agrees with the theoretical and empirical predictions. On the other hand, the relationship between the shaft rpm and torque is sensitive to the particle characteristics, and negative correlations were observed in some cases. Higher torque requirements imply higher tendency to the occurrence of screw blockage, as the driving torque to be delivered by the connected motor has a peak value that cannot be exceeded. In addition, higher torques at the same shaft rotating speed corresponds to higher energy consumption.

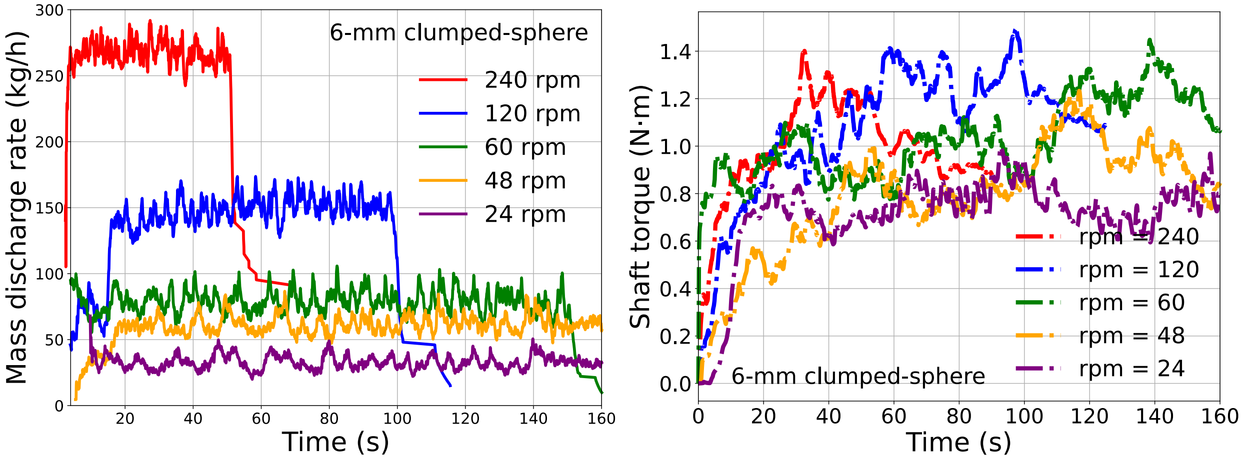

(a) (b)

Figure 5. Computed space-averaged mass discharge rate (a) and rolling average torque (b) versus time, using various shaft rotational speeds, for the 6-mm clumped-sphere particle model.

### 3.3 Impact of Crumbles Attributes on the Screw Feeder Performance

One of the objectives of this study was to investigate the impact of particle characteristics on the performance of the screw feeding of dry biomass. Figures 6(a), 6(b), and 6(c) demonstrate, respectively, the effect of particle size on the mass flow rate, the shaft torque, and specific energy consumption from both experiment and simulations using a shaft rotational speed of 48 rpm. In this regard, it should be borne in mind that the specific energy consumption (in the units of energy per unit mass) corresponds to the mechanical energy calculated based on the time-averaged shaft torque normalized by the mass flow rate. The three metrics used to evaluate the performance in the Acrison screw feeder test agree with the static AOR metric (see Figure 1) and demonstrate the enhanced flowability achieved by reducing the particle size of Crumbles from veneer to 2 mm instead of 6 mm. This is evidenced by the higher mass discharge rate and lower values for the driving shaft torque and specific energy consumptions in the case of the 2-mm particles. The potential for energy saving during the feedstock handling and feeding processes by reducing the particle size to 2 mm is obvious, as the specific energy consumption for the feeding of the 6-mm particles is roughly 8 times larger than the 2-mm particles. This saving in the operational cost can partially compensate for the higher comminution energy required to produce the 2-mm particles (Figure 1).

The DEM simulation results using cubic-shaped, clumped-sphere particle model show good agreement with experiments and effectively capture the experimentally observed trends. However, the existing marginal discrepancy between the predicted results and experiment, where the mass discharge rate is overpredicted (underpredicted) for the small (large) particle size indicates missing contribution from a particle feature that was not calibrated in the present study. Given the uniform shape and side length of the Crumbles, the observed differences suggest the importance of characterizing the particle surface roughness as an additional parameter in the construction of the DEM particle shape model. Another possible factor is the assumption made in the DEM simulations of mono-sized particles, while in the physical experiment some variation in the particle size exists. It should be noted that the observed particle size effects on the flowability of the dried Crumbles is not universal and implicitly depends on other influential parameters. For example, the authors reported previously a negligible impact of particle size on the static AOR in the case of dried Crumbles from wood chips that possess a needle-like shape [23]. Furthermore, unlike cohesionless particles, the particle size and the static AOR can move in tandem in the case of cohesive particles, see, for example, the empirical model developed by Elekes and Parteli [71]. This is usually important in the case of fine powders with particle size in the range of microscale, as Van der Waals forces play a key role in the particle-particle interactions, and the case of very wet particles due to the moisture content-induced capillary forces. For these scenarios, incorporation of attractive forces into the DEM contact force model will be necessary for reliable predictions.

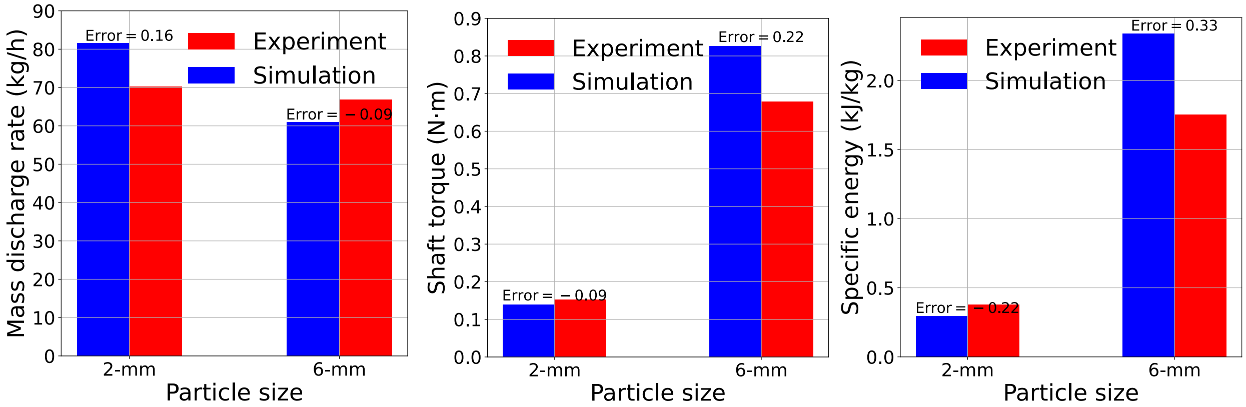

(a) (b) (c)

Figure 6. Particle size impact on the considered CQAs at a shaft rotational speed of 48 rpm: (a) mass discharge rate, (b) shaft torque, and (c) specific energy consumption from both experiment and DEM simulations. Relative errors between simulation and experimental results are shown atop of the bars.

The effect of the particle size distribution was also studied using DEM simulations by composing a binary mixture using the 2-mm and 6-mm particle sizes, which were seeded randomly into the hopper during the packing stage with equal fractions of total particle number. In Figures 7(a), 7(b), and 7(c), the change in the screw performance metrics (mass discharge rate, shaft torque, and specific energy consumption, respectively) with shaft rpm for the wide PSD case is compared with the two monodispersed systems consisting of the 2-mm and 6-mm particles. In agreement with the experimental observations made by Dai and Grace [72] during testing the effects of material attributes on the flow behavior of woody biomass feedstocks in screw feeders, the bi-disperse particle system representing a broader PSD exhibited the highest values for shaft torque and thus indicates an increase in the likelihood of screw blockage. Moreover, the torque requirements for transporting the 2-mm particles are remarkably smaller than the 6-mm particles for all shaft rotating speeds. The increase in the shaft rpm caused slight increase in the shaft torque for the three different cases. However, the difference between the shaft torque for the 6-mm and the mixed two-sizes case becomes smaller at the higher shaft rotational speed of 60 rpm. Although for all cases the mass discharge rate showed strong positive correlation with the shaft rpm, the rate of change is different. For example, in contrast to the 6-mm particle size and the binary mixture cases, the 2-mm particle size simulations show deviation from the linear regime at the higher speed of 60 rpm. Moreover, the mass discharge rates for the binary mixture are similar to the case of 6-mm particle size, except for the 60-rpm speed, as it becomes smaller. Like the two other performance metrics, further shaft rotating speed causes higher specific energy consumption for the three different cases.

To understand the reasons for the above observed behavior, the interplay between different acting mechanisms needs to be analyzed. For this purpose, a distinction should be made between the static effects arising from geometrical considerations and the dynamic effects that are correlated with the magnitude of the shaft rotating speed. Particle shape, size, and size distribution play an important role in determining the hopper discharge rate as well as the maximum packing fraction of the screw region. For the same particle shape, polydisperse system can achieve higher random packing fraction than mono-sized system [73], as finer particles can fit into the space between larger particles. At the same time, the empirical formula by Beverloo [74] and DEM simulations predict that hopper discharge rate for monodisperse system increases nonlinearly with the decrease in the particle size [75]. The relation follows a power law with an exponent that is higher than 2. Mixing the two-particle sizes gives rise to segregation phenomena, which occur due to the difference in any of several physical properties (particle size, shape, density, etc.). Because of segregation, several flow patterns can develop that have an adverse effect on the handling process and final product quality. In gravity-driven segregation, two competing mechanisms are active, namely, the kinetic sieving and the squeeze expulsion [76]. Kinetic sieving refers to the fine particles percolating downward through the porous network formed by the gaps between the coarser particles, while squeeze expulsion leads to upward flux. When accompanied by velocity shear, a secondary segregation can be triggered in the lateral direction (radial segregation). Several experimental and DEM studies reported improved hopper mass discharge rate by adding fine particles to the coarse monodisperse granular systems [75,77,78]. Increasing the mass fraction of the fine particles resulted in increasing the mass flow rate. In addition, particle segregation was observed with relative increase in the fine particle fraction near to the end of the collected mass flow. Although these remarks are based on flow under the action of gravity, they are consistent with several findings for the screw feeder made in this work. For example, the 2-mm particle system achieved much higher flow rate than the 6-mm counterpart. Given the mass fraction of the 2-mm particles in the binary mixture is less than 3.6 %, no change in the mass flow rate was observed in that case as compared with the 6-mm particle size case. However, segregation was observed with higher presence of the 6-mm particle at the flow front. For example, the initial discharged mass flux was depleted in the 2-mm particles, while the delayed flux was enriched in the finer (2-mm) particles. These remarks cannot help interpreting the behavior observed at the 60-rpm shaft speed though.

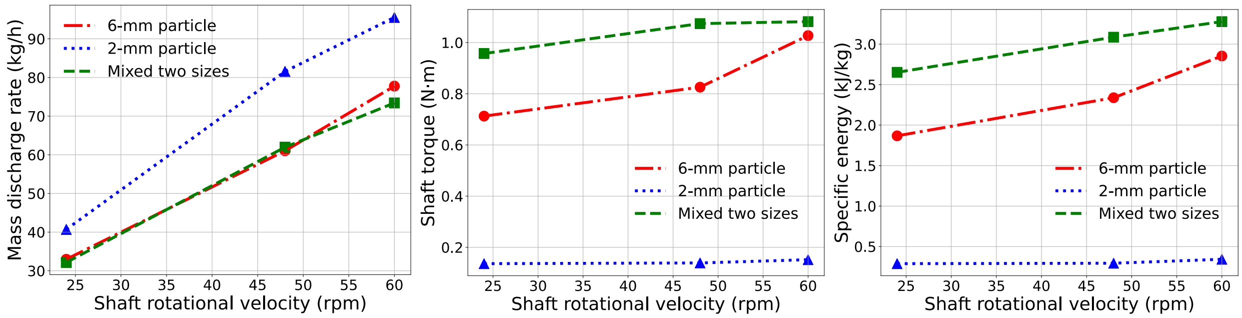

(a) (b) (c)

Figure 7. Impact of the shaft rotational speed on the considered CQAs for different particle sizes from DEM simulations: (a) mass discharge rate, (b) shaft torque, and (c) specific energy consumption.

To shed light on the reason for the higher shaft rotational speed behavior, the dynamic effects induced by shaft rotation need to be considered. Insights gained from the rotating drum test can be helpful in this regard. In the rotating drum, by increasing the drum rotational speed, the granular material undergoes different flow pattern. In ascending order, encountered regimes include slipping, slumping, rolling, cascading, cataracting (fluidization), and centrifuging [57,59]. Higher rotating speeds lead to higher dynamic AOR, porosity (lower coordination number), and mean collision energy [58,79]. The rotational speed at which the transition between two consecutive regimes takes place changes with particle features. In the case of screw conveyor, the rotating screw induces a solid body rotation. Nevertheless, the interparticle viscous friction is another mechanism that can change the mode of the particle vortex motion. Wang et al. [38] used DEM simulations to analyze the local rotational, translational, and configurational temperatures of particles moving in a screw conveyor for different shaft rpm. They reported further shaft rotational speed instigates turbulence associated with particle oscillation in the plane normal to the flow direction. On the other hand, weaker influence on the translational temperature was observed. The observed turbulence at higher shaft rpm implies higher collision frequency, as the amount of imparted energy becomes sufficiently high to increase the amplitude of the particle lateral vibration to a degree that overlaps with the active region for contiguous particles. This, in turn, is responsible for the decrease in particle coordination number and a reduction in the attainable screw filling fraction, which can also have a negative feedback effect on the hopper discharge by enhancing recirculation at the hopper outlet. Accordingly, this mechanism is responsible for the onset of the sublinear regime in the 2-mm particle mass throughput profile. This also affects the mass discharge rate for the binary system at 60 rpm and cause the shaft torque to level off. The lower mass throughput of the 6-mm particles system indicates a smaller value for the screw filling fraction than the 2-mm. Consequently, the onset of the sublinear behavior for this case requires higher screw shaft speeds, which can be interpreted in terms of the amplitude of the lateral particle vibration that needs to become large enough to effectively resist the axial flow via the increase in the frequency of binary collision. Higher shaft torques observed in the case of the binary systems can be attributed to the additional angular momentum needed to enable the solid body rotation, which is required to overcome the effect of the mechanical interlocking mechanism with smaller particles acting like a glue between larger particles. Figures 8 supports this conclusion. The high peak observed at a pair separation distance of 2 mm in the profile of partial radial distribution function for the anisometric base spheres comprising the 2-mm and 6-mm clumped-sphere particles in the binary system confirms this behavior. This is because the 2-mm pair separation distance corresponds to the situation where the 2-mm and 6-mm particles are touching each other. Figures SC shows a snapshot of the spatial arrangement of the bi-disperse system particles around the screw shaft. This indicates 2-mm particles preference to flow into the interstitial space between the 6-mm particles, which leads to the mechanical interlocking.

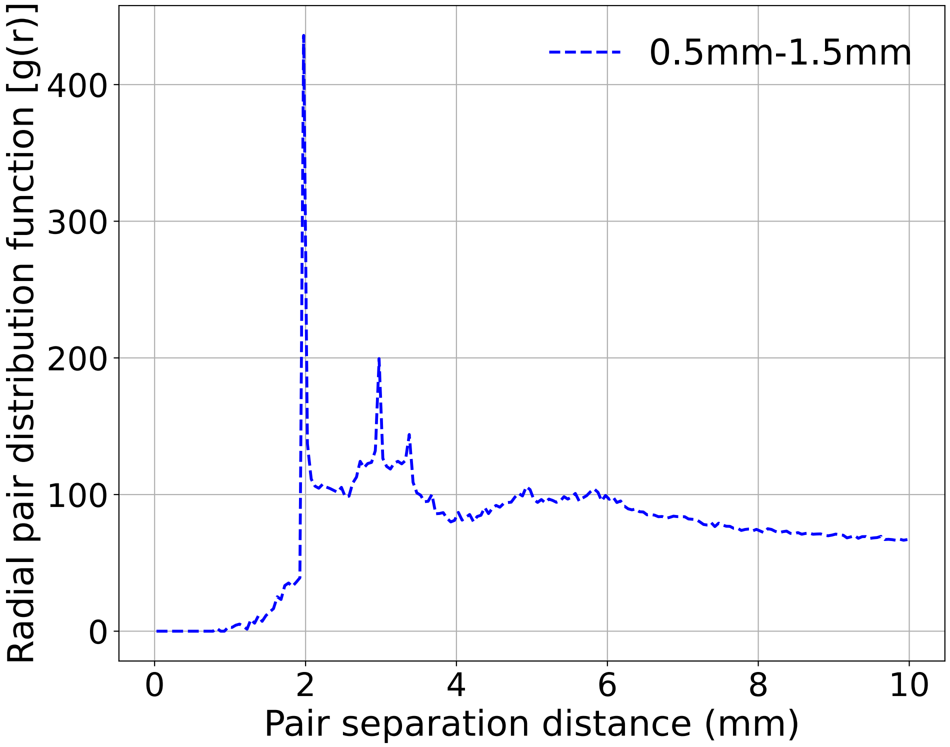

Figure 8. Partial radial pair distribution function versus pair separation distance between the base spheres comprising the 2-mm clumped-sphere particles (radius = 0.5 mm) and the 6-mm particles

(radius = 1.5 mm) obtained from the simulation of the binary system with a shaft rotational speed of 60 rpm.

## 3.4 Particle Shape and Hopper Filling Height Effects and Coarse-grained Contact Model

Like particle size, particle shape has a significant influence on the flow behavior of the granular materials. For example, Zhou et al. [34] used stress analysis from DEM simulations of the bottomless cylinder test to show the remarkable particle shape impact on the magnitude of the pairwise normal contact force. Among the studied shapes, spherical particles achieved the smallest stress level with almost constant value for the normal pressure distribution in the central region of the formed heap. Contrarily, non-spherical particles exhibited a more pronounced stress dip. Likewise, particle shape was found to have a substantial impact on the hopper flow. Using ellipsoid particles, Liu et al. [80,81] found spherical particles to achieve the highest discharge rate in cylindrical hoppers. The authors studied previously the AOR of 6-mm single sphere particle and found it to be smaller than the 6-mm clumped-sphere particle used here (32° versus 38°), which suggests better free-surface flow properties [23]. In this work, the effect of the particle shape is studied by comparing the performance of the screw feeder using 6-mm single sphere particle with the 6-mm cubic shape (using the clumped-sphere model). Figure 9 shows the results for the two cases. Interestingly, the spherical particles exhibited remarkably lower values for the mass discharge rate and the shaft torque. The lower mass discharge rate for spherical particles can be explained in terms of the higher number of cubic particles that can be fit within the enclosed volume for the same packing fraction. Similar observation was reported by Sun et al. [82] in their investigation of the particle shape effect on the conveying behavior in a screw conveyor. They also observed the strong correlation between the collision frequency and the shaft rotational velocity. So, the transportation capacity for cubic particles in a screw conveyor is higher than the spherical particles. On the other hand, the several orders of magnitude difference in the shaft torque makes the transportation cost of the spherical particles much cheaper and requires the use of powerful motors in the case of cubic particles to avoid screw blockage and lack of flow scenarios. This can be attributed to the surface roughness induced interlocking mechanism in the case of the clumped-sphere particle shape, which makes particle rotation much harder, and the larger area between the cubic particle and the screw shaft resulting in significant increase in the magnitude of the friction forces. as well as the higher torque and momentum transfer efficiency achieved with the clumped-sphere model as compared to the single sphere particle. Although the shaft torque profile for the clumped-sphere reaches a plateau, the single-sphere particle shows a decrease in the shaft torque at higher rpm. This indicates that the centrifuging forces dominates, which results in higher efficiency in the momentum and energy transfer through the granular medium. This is evidenced by the decrease in the specific energy consumption for the single sphere model in Figure 9(c). The smooth surface of the spherical particles with high symmetry degree and no presence of edges and the absence yields the transition in the concerted particle rotation mode from random to directed by the act of external forces more possible.

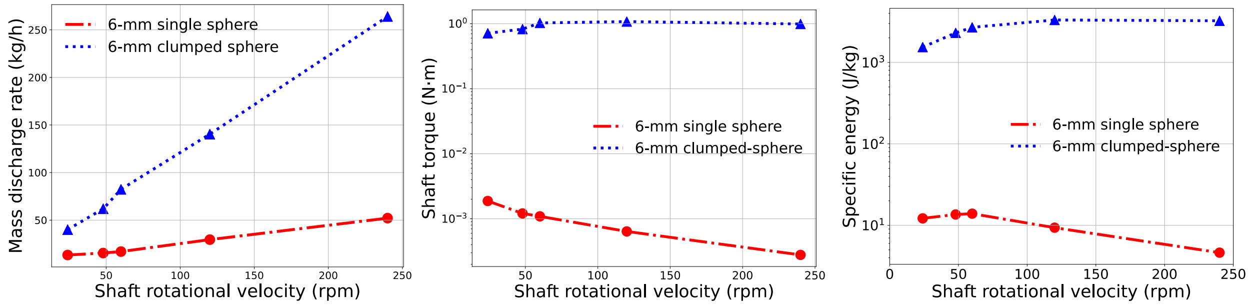

(a) (b) (c)

Figure 9. Impact of the DEM particle shape on the computed CQAs for a particle size of 6 mm at different shaft rotational speeds: (a) mass discharge rate, (b) shaft torque, and (c) specific energy consumption.

The stress-strain behavior of milled pine under stress consolidation exhibits hysteresis and strain hardening response. Chen et al. [65] developed a nonlinear hysteretic contact model for the normal contact force of milled pine, which was calibrated and validated using the experimental cyclic loading-unloading axial compression data for loblolly pine. In contrast to linear hysteretic models, the developed model employs history-dependent loading and unloading stiffnesses that continuously increase with repeating the cycle of interparticle overlapping and separation. This allows for accurate prediction of the bulk compressibility and constrained moduli for milled pine. In conjunction with single sphere particle shape model, this contact model was used to successfully predict the hopper flow behavior of milled pine and achieved good agreement with experiment [12]. To investigate the applicability of this approach to our problem, the nonlinear hysteretic model was used to replace the normal contact force in the Hertz-Mindlin model and employed along with the 6-mm single sphere particle in the simulations of the Acrison screw feeder. Figure 10 compares the prediction of this contact model for the three-performance metrics with the Hertz-Mindlin model prediction. The impact of the hysteretic model on the flow rate is less obvious when compared with the torque profile. At least an order of magnitude increase in the shaft torque was achieved using this model. Interestingly, the shaft torque profile reveals a non-monotonic relation with the shaft rpm, and a peak exists about 60 rpm. The increase in the torque magnitude can be attributed to the higher energy dissipation arising from the hysteresis loss. Apparently, the relative contribution of hysteresis loss to the energy dissipation decreases for higher rpm due to the decrease in the particle coordination number, and hence viscous dissipation becomes more important.

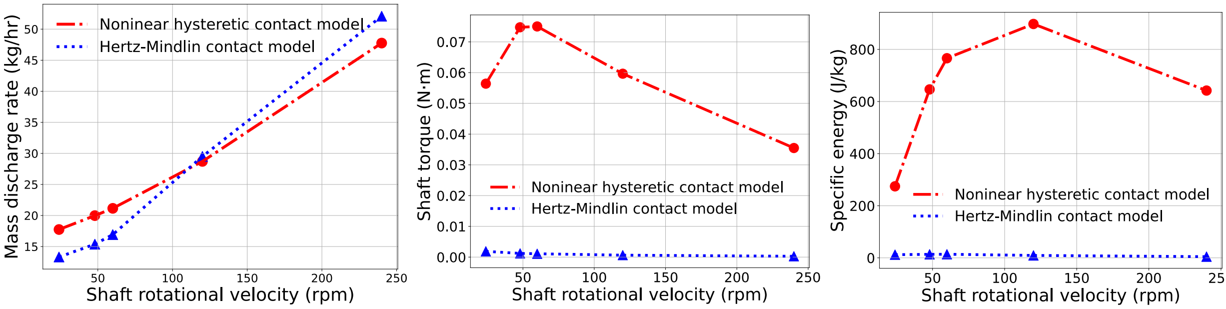

(a) (b) (c)

Figure 10. Impact of the DEM contact model on the computed CQAs using 6-mm single sphere particle at different shaft rotational speeds: (a) mass discharge rate, (b) shaft torque, and (c) specific energy consumption.

To better analyze the complex behavior of the shaft torque and the impact of the shaft rpm, it is more helpful to display the time series of the shaft torque in the frequency domain. Figures 11(a) and 10(b) depict the amplitude of the shaft torque profiles using different values for rpm in the frequency domain, by applying fast Fourier transform (FFT), for the 6-mm clumped-sphere and single sphere particle shape models, respectively. It should be noted that the plots in Figure 11(b) corresponds to the results obtained from the simulations that invoked the nonlinear hysteretic contact model. Figure 11(a) demonstrates the existence of a pronounced resolved resonance located at the corresponding shaft rotation frequency for each rpm, which possesses the highest magnitude within each profile. Obviously, the amplitude of the observed resonance is inversely proportional to the shaft rotation frequency. This indicates that rotational speed of the shaft is the main source for the oscillation in the shaft torque temporal profile. Other unresolved and/or low-magnitude resonances are also apparent in each profile, which are independent of the shaft rpm and contribute to the torque oscillations as well. Possible origins might include geometrical factors such as the screw conveyor pitch-to-diameter ratio. Wang et al. [38] reported similar correlation between particle flow fluctuations and screw speed. All other simulations cases in this work exhibited behaviors like those in Figure 11(a), except for the case of the hysteretic contact model. Figure 11(b) shows a resonance absorption-like phenomenon at an intermediate speed (60 rpm) with the magnitude of the pronounced resolved resonance (marked in the figure) being the highest among the different rpm values, see Figure 11(c) for comparison. From that figure, the two calculated correlation coefficients, namely Pearson and Spearman's correlation coefficients confirm the strong negative correlation between the highest resolved peak amplitude and the shaft rpm within the investigated range of speeds for simulation cases other than the hysteretic contact model. In contrast, the magnitude of the calculated correlation coefficients for the hysteretic contact model are remarkably smaller due to the resonance behavior. Several studies considered the resonance flow phenomena in granular systems [83–85], particularly in non-cohesive, strongly dissipative systems driven by external forces. The observed behavior suggests an interference between the nonlinear hysteretic damping that depends on the number of the loading cycles (which is directly correlated with the collision frequency) and the shaft rpm. This interference leads to a magnification in energy dissipation.

In addition to screw blockage, loss of flow in a screw feeder can also result from hopper arching or bridging. There are two main flow regimes usually encountered during the discharge of granular systems from the hopper, namely, the mass flow and the funnel flow [12,14]. In the mass flow regime, which exhibits a first-in, first-out pattern, the whole granular bed remains in motion. Usually, this is the most favorable regime for many applications. Certain hopper design parameters should be adopted to guaranty mass flow, see for example [12,14]. In this work, the two selected hopper geometries are steep enough and have wide enough opening such that continuous mass flow was always observed. Thus, the main effective difference between the two hoppers is the filling height. Figures 12(a), 12(b), and 12(c) illustrate the hopper filling height effects on the mass flow rate, shaft torque, and the specific energy consumption, respectively. The displayed results belong to set of simulations using the hysteretic contact model in conjunction with the single sphere particle shape model. The mass flow rate is barely affected by the hopper filling height. Contrarily, the filling height has a clear impact on the shaft torque, which reflects higher propensity for screw blockage with larger hopper filling height. These remarks are consistent with what reported in the literature, see for example [43,72]. From Figure 12(c), it can be inferred that particle transportation cost, in terms of the specific energy consumption, becomes higher with larger hopper filling height. This suggests the use of less-steep hopper could be more beneficial to save on particle transportation energy while retaining the same transportation capacity. However, this needs to be constrained by the design guidelines for the minimum hopper inclination angle that maintain the particle flow in the hopper in the mass flow regime. Interestingly, the short hopper resembles a resonance flow phenomenon with shaft torque being the lowest at 60 rpm.

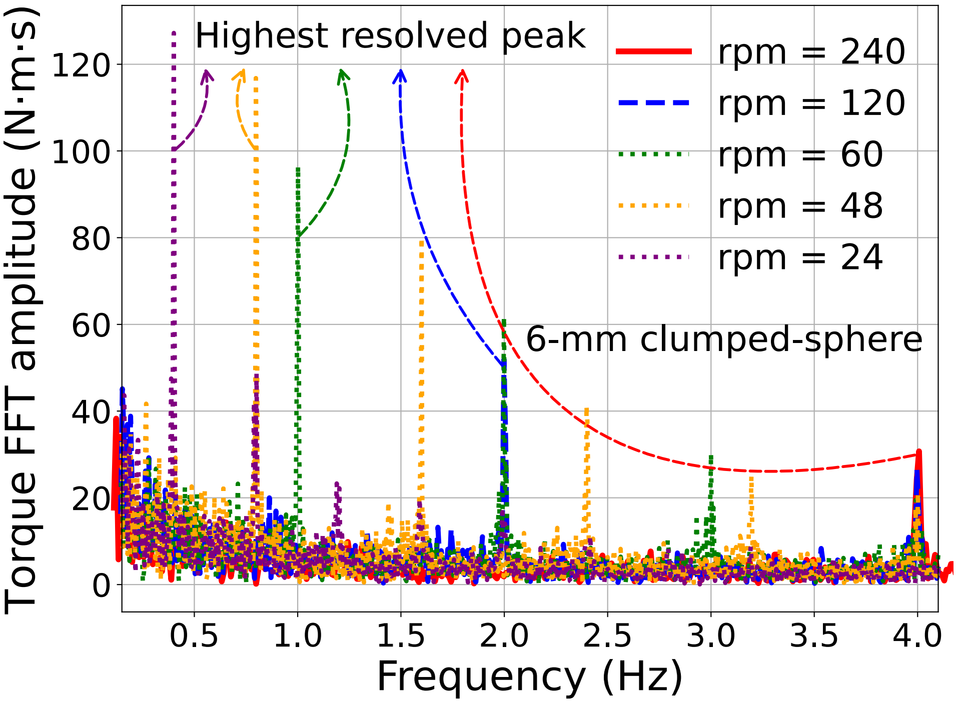
Highest resolved peak
rpm = 240
rpm = 120
rpm = 60
rpm = 48
rpm = 24
6-mm clumped-sphere
Torque FFT amplitude (N·m·s)
0
20
40
60
80
100
120
Frequency (Hz)
0.5
1.0
1.5
2.0
2.5
3.0
3.5
4.0

(a)

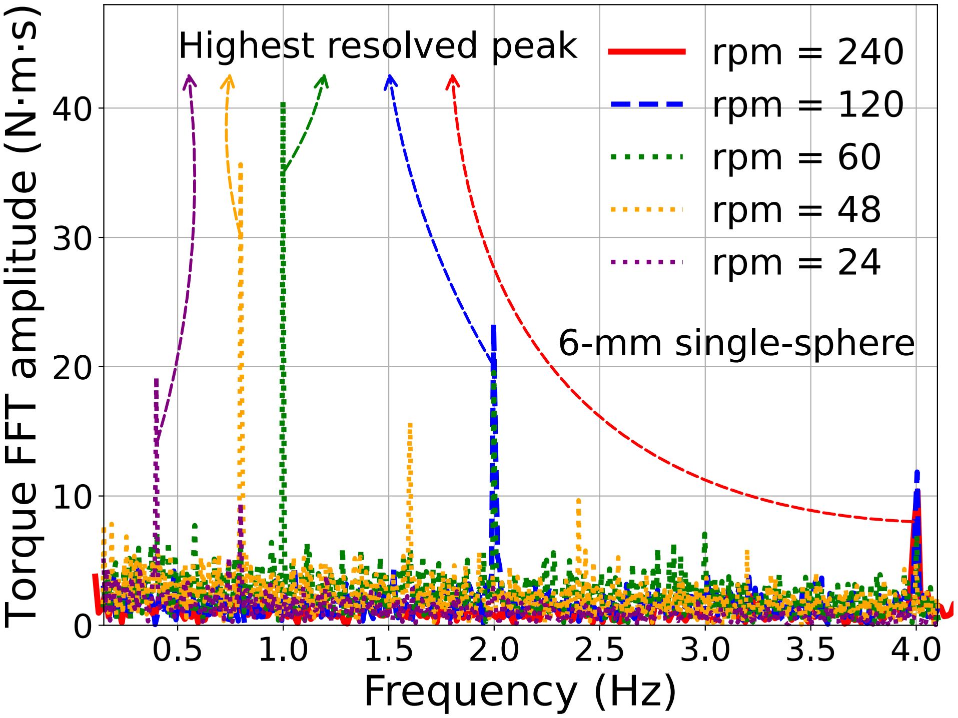
Highest resolved peak
rpm = 240
rpm = 120
rpm = 60
rpm = 48
rpm = 24
6-mm single-sphere
Torque FFT amplitude (N·m·s)
0
10
20
30
40
Frequency (Hz)
0.5
1.0
1.5
2.0
2.5
3.0
3.5
4.0

(b)

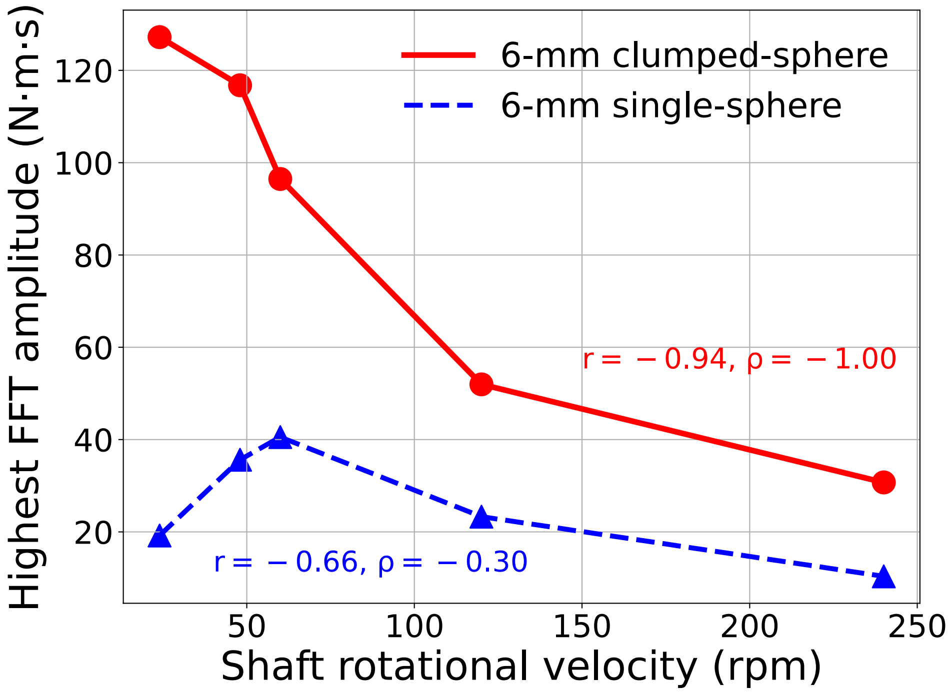

(c)

Figure 11. Amplitudes of the Fast Fourier Transformation (FFT) of the space-averaged shaft torque versus frequency for the DEM screw feeder simulations of five different shaft rotational speeds using the 6-mm clumped-sphere (a) and 6-mm single-sphere (b) particle models. (c) shows the highest resolved peak amplitude versus shaft rotational speeds from (a) and (b) along with the calculated Pearson (r) and Spearman's (ρ) correlation coefficients.

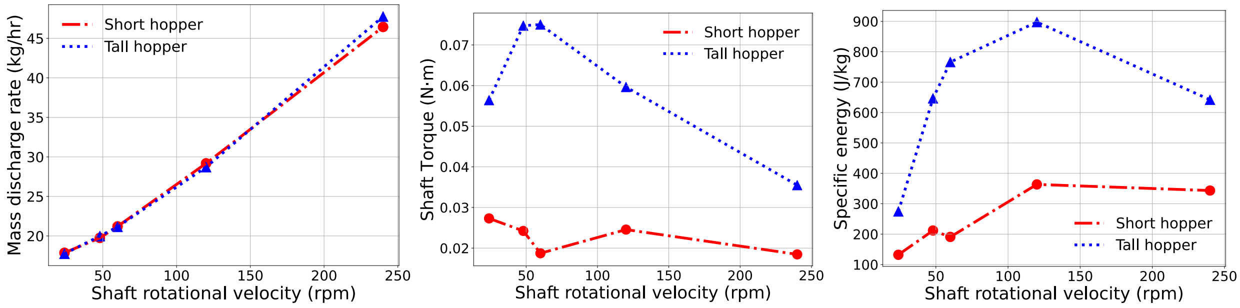

(a) (b) (c)

Figure 12. Impact of hopper dimension on the computed CQAs using 6-mm single sphere particle at different shaft rotational speeds: (a) mass discharge rate, (b) shaft torque, and (c) specific energy consumption.

### 3.5 Analysis of The DEM Simulations Computational Cost on HPC

As noted earlier, all simulations were performed on HPC via LIGGGHTS-INL. Sawtooth, the latest INL supercomputer, was utilized, which have current LINPACK rating of more than six petaflops. Sawtooth comprises 2079 compute nodes and uses Linux CentOS 7 operating system. Each compute node consists of 2 Intel Xeon 8268 CPUs with 192 GB of RAM, while each CPU contains 24 HPE SGI 8600 cores. This section will provide the computational cost of different simulations cases in terms of the total computational time in the unit of Processors-hours, which is calculated by multiplying the CPU time by the total number of the used CPU cores.

Figure 13(a) depicts the relation between the computational cost and the shaft rpm for the 6-mm clumped-sphere and single-sphere particle shape models using Hertz-Mindlin contact model. Surprisingly, the computational cost for the clumped-sphere models is either the same or slightly higher than the single sphere model. This can be explained by considering the entire physical time needed to completely empty the screw feeder in each case, i.e., the total number of timesteps. Given the smaller mass flow rate for the single sphere, longer physical time is needed to simulate this case, which compensates for the additional computational cost per timestep needed in the case of the clumped-sphere models. Another remark can be made from that figure that is related to the exponential increase in the computational cost by decreasing the shaft rpm. This can be attributed to the higher coordination number at lower rpm, which is associated with more populous neighbor lists and higher computational cost for force calculations.

Figure 13(b) shows the computational cost (left axis) and the system size in terms of the total number of bases spheres (right axis) at a shaft rotation speed of 48 rpm for the clumped-sphere particle shape model with three different particle sizes corresponding to the 2-mm, the 6-mm, and the binary mixture. The average particle radius (4 mm) is used for the binary mixture. As would be expected, the computational cost for the 2-mm particle size system is the highest due to its large size (~ 7 million base spheres). However, if a system-size agnostic metric is used, e.g., by normalizing the computational cost by the system size, the computational cost for the 2-mm particle size system becomes the cheapest (or in other words, the most efficient). On the other hand, the binary mixture simulation unexpectedly outperforms the 6-mm mono-sized system simulation. This could be related to the stabilization effects introduced by the 2-mm particles acting as a glue between the 6-mm particles. This results in the neighbor list updates becomes less frequent than the 6-mm monodisperse case. In addition, by using the same normalized metric and noting the superior performance of the 2-mm particle versus the 6-mm particle, the cheaper computational cost for the binary mixture as compared with the 6-mm case becomes less surprising.

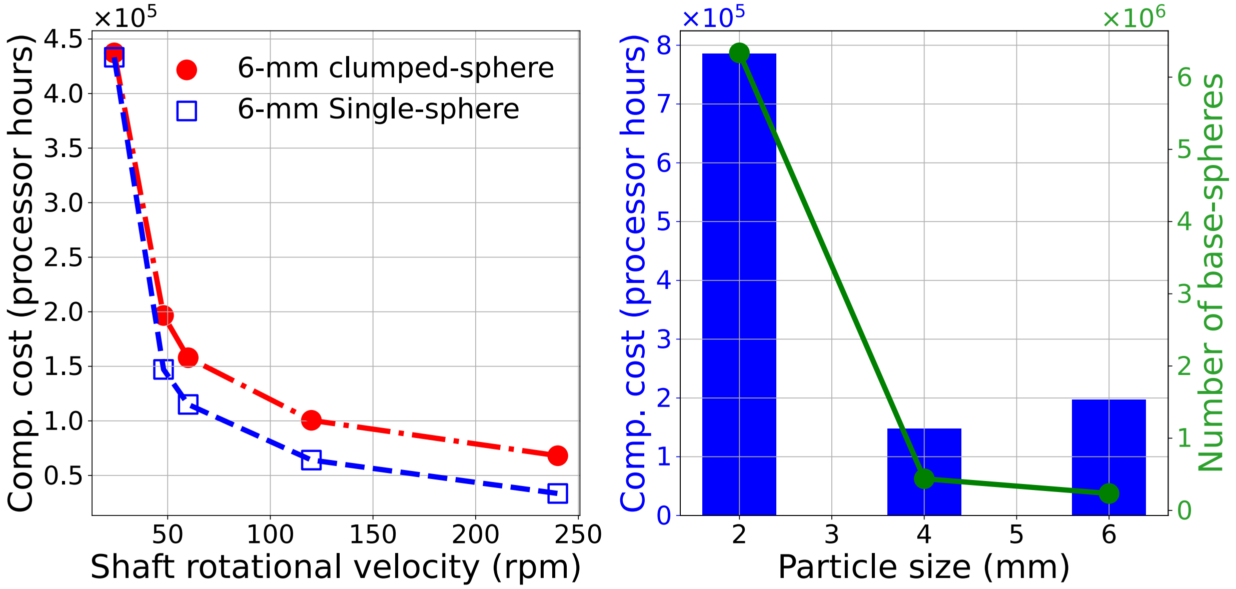

(a) (b)

Figure 13. Computational cost of the DEM simulations for different particle shape models and sizes: (a) the total computational cost versus the shaft rotational speed for clumped-sphere and single sphere DEM particles of 6-mm size. (b) the computational cost for DEM simulations of different clumped-sphere particle sizes at a shaft rotational speed of 48 rpm (left axis) and the total

number of seeded base-spheres (i.e., the total number of DEM particles multiplied by the number of base-spheres comprising a clumped-sphere particle) in each of these simulations (right axis).

## 4 Summary and Future Outlook

Despite of the abundance and cheap cost of biomass materials in their raw form, problems related to the feeding and handling of lignocellulosic biomass feedstocks represent substantial barriers that need to be eliminated or sufficiently characterized to enable commercial-scale deployment of bioenergy technologies. Poor flowability due to the high variability in materials attributes is one of the main reasons for the underperformance of many materials handling unit operations. Biomass feedstocks flowability is also affected by particle morphology resulting from the milling conditions.

Preprocessing and materials handling involve energy intensive processes. Thus, developing mitigating strategies requires identifying the underlying mechanisms controlling the flow behavior of this biomass feedstocks to determine critical parameters. This can aid in the optimization of preprocessing unit operations and engineering favorable flowability of biomass in feeding and handling. The present work sought quantitative assessment of the effect of particle characteristics of rotary sheared Douglas fir particles on the performance of a pilot-scale, horizontal screw feeder unit (Acrison®) using a combined computational and experimental approach. A state-of-the-art comminution unit (Forest Concepts Crumbler® rotary shear system) was used to produce dried cubic Crumbles from veneer at two different nominal sizes (2 mm and 6 mm). Three CQAs (mass flow rate, shaft torque, and specific energy consumption) were used as the performance metrics to elucidate the relation between materials attributes, operation parameters, and material flowability. DEM simulations were also conducted to further investigate the impact of additional CMAs (particle shape, PSD, and contact model) and CPPs (shaft rotational speed and hopper dimension) on the chosen CQAs.

In agreement with the static AOR metric, the three metrics used in the Acrison screw feeder test confirmed that the 2-mm Crumbles from veneer particle exhibits superior flowability as compared to the 6-mm counterpart. In addition, DEM simulation results using the clumped-sphere particle model has shown good agreement with the experiment. The lower transportation cost for the 2-mm particle size can partially compensate for the higher comminution cost (in terms of specific energy consumption). Moreover, mixing the two particle sizes (to resemble a wide PSD) resulted in poorer flowability than the 6-mm particle size due to the higher screw blockage propensity, which proves the flowability enhancement achieved by the characteristic narrower PSD of the Crumbles. From different screw auger-feeder shaft rotational speeds considered in DEM simulations, it is concluded that higher rpm leads to higher mass flow rate at the cost of higher specific energy consumption. This is mainly ascribed to the transition in the rotational flow pattern at higher rpm with increased energy dissipation originating from higher collision frequency within the auger. By comparing DEM simulation results for a single sphere particle shape with the clumped-sphere model, it was found that the driving shaft torque is underpredicted by several orders of magnitude. In addition, the screw feeder transportation capacity is higher for the cubic particle shape. By using nonlinear hysteretic contact model that is experimentally calibrated for milled conifer wood in conjunction with single sphere particle shape model, marginal improvement in the predicted shaft torque was achieved. However, the mass flow rate remained unchanged. This suggests the surface roughness induced mechanical interlocking between contacting particles is the dominant mechanism in determining the driving torque. The complex nonlinear dynamics associated with the nonlinear hysteretic contact model gave rise to an emergent phenomenon with resonance flow-like behavior. Experimental investigation is needed to verify the authenticity of the observed behavior. Changing hopper filling height for single sphere particle model showed no impact on the mass flow rate. Nonetheless, larger hopper filling heights is positively correlated with higher risks of screw conveyor blockage. All remarks concluded from the DEM simulation results were found consistent with findings from other studies reported in literature. It should be noted that caution must always be exercised when making such comparison due to the inherent uncertainties resulting from uncontrolled experimental conditions.

Although using elaborate contact models that capture the characteristic mechanical response of the granular biomass materials seems as a promising approach, at the time being simpler contact models such as Hertz-Mindlin in conjunction with particle shape model mimicking realistic particle features better predicts the performance metrics in the screw feeder. This serves as evidence of the importance of adopting the realistic particle features to reliably simulate biomass granular flow under wide range of loading conditions. The analysis of the computational cost of the clumped-sphere model demonstrates the computational efficiency of force calculations and contact detection. The increase in the computational cost by adopting clumped-sphere model at mesoscale is moderate when compared with single sphere particle shape. This higher cost is still affordable and entirely justified by the high-fidelity nature of clumped-sphere models originating from their capability to account for different aspects of particle characteristics, which admits capturing the underlying physics.

Several future directions can be considered to improve the model predictability of the granular flow behavior for biomass feedstocks. These include accurate characterization of particle characteristics to account for the uncertainties in the measured features and adopting surface roughness as an additional parameter in calibrating DEM particle models. In addition, more efforts are needed to develop reliable and experimentally validated contact models for the moisture content impact on the interparticle interaction that incorporate the complex interplay between other involved factors such as the intraparticle structure, porosity, and temperature. Moreover, more experimental work is needed for accurate calibration of the viscoplastic response of biomass feedstocks and different modes of fracture. Physical experiments are also necessary to quantitatively assess the effect of different particle size distributions on the flowability of particulate systems. Furthermore, a comprehensive technoeconomic analysis to identify the optimal process parameters is still lacking. Accomplishing this task dictates a thorough quantification of the impact of critical material attributes on different feedstock aspects and must use modelling approaches in tandem with experimentations.

## Acknowledgments

Funding: This research is supported by the U.S. Department of Energy (DOE), Office of Energy Efficiency and Renewable Energy (EERE), Bioenergy Technologies Office (BETO), the Consortium for Computational Physics and Chemistry (CCPC) and the Feedstock Conversion and Interface Consortium (FCIC), under DOE Idaho Operations Office with Contract No. DE-AC07-05ID14517. This research made use of the resources of the High Performance Computing Center at Idaho National Laboratory, which is supported by the Office of Nuclear Energy of the U.S. Department of Energy and the Nuclear Science User Facilities under Contract No. DE-AC07-05ID14517. Any opinions, findings and conclusions, or recommendations expressed in this material are those of the authors and do not necessarily reflect those of the DOE or the U.S. Government.

The authors would thank Dr. Feiyang Chen of Clemson University for generating the STL surface mesh files for the Acrison screw feeder system.

## References

[1] I. Renewable Energy Agency, Global Energy Transformation: A Roadmap to 2050, 2018. www.irena.org.

[2] O. of E.E. and R.E.Tech.Rep. U.S. Department of Energy Bioenergy Technologies Office, Biorefinery Optimization Workshop Summary Report, 2016.

[3] P.N. Ciesielski, M.B. Pecha, A.M. Lattanzi, V.S. Bharadwaj, M.F. Crowley, L. Bu, J. V. Vermaas, K.X. Steirer, M.F. Crowley, Advances in Multiscale Modeling of Lignocellulosic Biomass, ACS Sustain Chem Eng. 8 (2020) 3512–3531. https://doi.org/10.1021/acssuschemeng.9b07415.

[4] O. Oyedeji, P. Gitman, J. Qu, E. Webb, Understanding the Impact of Lignocellulosic Biomass Variability on the Size Reduction Process: A Review, ACS Sustain Chem Eng. 8 (2020) 2327–2343. https://doi.org/10.1021/acssuschemeng.9b06698.

[5] K.L. Kenney, W.A. Smith, G.L. Gresham, T.L. Westover, Understanding biomass feedstock variability, Biofuels. 4 (2013) 111–127. https://doi.org/10.4155/bfs.12.83.

[6] W. Stelte, A.R. Sanadi, L. Shang, J.K. Holm, J. Ahrenfeldt, U.B. Henriksen, Recent developments in biomass pelletization – A review, Bioresources. 7 (2012) 4451–4490. https://doi.org/10.15376/biores.7.3.4451-4490.

[7] X. Gao, L. Lu, M. Shahnam, W.A. Rogers, K. Smith, K. Gaston, D. Robichaud, M. Brennan Pecha, M. Crowley, P.N. Ciesielski, P. Debiagi, T. Faravelli, G. Wiggins, C.E.A. Finney, J.E. Parks, Assessment of a detailed biomass pyrolysis kinetic scheme in multiscale simulations of a single-particle pyrolyzer and a pilot-scale entrained flow pyrolyzer, Chemical Engineering Journal. 418 (2021). https://doi.org/10.1016/j.cej.2021.129347.

[8] Y. Lu, W. Jin, J. Klinger, S. Dai, Flow and Arching of Biomass Particles in Wedge-Shaped Hoppers, ACS Sustain Chem Eng. 9 (2021) 15303–15314. https://doi.org/10.1021/acssuschemeng.1c05628.

[9] W. Jin, J.J. Stickel, Y. Xia, J. Klinger, A Review of Computational Models for the Flow of Milled Biomass Part II: Continuum-Mechanics Models, ACS Sustain Chem Eng. 8 (2020) 6157–6172. https://doi.org/10.1021/acssuschemeng.0c00412.

[10] M. Rackl, F. Top, C.P. Molhoek, D.L. Schott, Feeding system for wood chips: A DEM study to improve equipment performance, Biomass Bioenergy. 98 (2017) 43–52. https://doi.org/10.1016/j.biombioe.2017.01.003.

[11] Y. Xia, J.J. Stickel, W. Jin, J. Klinger, A Review of Computational Models for the Flow of Milled Biomass Part I: Discrete-Particle Models, ACS Sustain Chem Eng. 8 (2020) 6142–6156. https://doi.org/10.1021/acssuschemeng.0c00402.

[12] F. Chen, Y. Xia, J. Klinger, Q. Chen, Hopper discharge flow dynamics of milled pine and prediction of process upsets using the discrete element method, Powder Technol. 415 (2023) 118165. https://doi.org/10.1016/j.powtec.2022.118165.

[13] E.W. Merrow, Problems and progress in particle processing, Chemical Innovation. 30 (2000) 34–41.

[14] Y. Lu, W. Jin, N. Saha, J.L. Klinger, Y. Xia, S. Dai, Wedge-Shaped Hopper Design for Milled Woody Biomass Flow, ACS Sustain Chem Eng. (2022). https://doi.org/10.1021/acssuschemeng.2c05284.

[15] T.L. Westover, D.S. Hartley, Biomass Handling and Feeding, in: Advances in Biofuels and Bioenergy, InTech, 2018. https://doi.org/10.5772/intechopen.74606.

[16] J. Mark, N.T. Gray, Annual Review of Fluid Mechanics Particle Segregation in Dense Granular Flows Granular avalanche: a shallow gravity-driven free-surface flow of grains, Annu. Rev. Fluid Mech. 50 (2018) 407–433. https://doi.org/10.1146/annurev-fluid-122316.

[17] D. Bonn, M.M. Denn, L. Berthier, T. Divoux, S. Manneville, Yield stress materials in soft condensed matter, Rev Mod Phys. 89 (2017). https://doi.org/10.1103/RevModPhys.89.035005.

[18] R. Navar, J.H. Leal, B.L. Davis, T.A. Semelsberger, Rheological effects of moisture content on the anatomical fractions of loblolly pine (Pinus taeda), Powder Technol. 412 (2022). https://doi.org/10.1016/j.powtec.2022.118031.

[19] C.J. Dibble, T.A. Shatova, J.L. Jorgenson, J.J. Stickel, Particle morphology characterization and manipulation in biomass slurries and the effect on rheological properties and enzymatic conversion, Biotechnol Prog. 27 (2011) 1751–1759. https://doi.org/10.1002/btpr.669.

[20] G. Peter Van Walsum, S.G. Allen, M.J. Spencer, M.S. Laser, M.J. Antal, L.R. Lynd •'i, Conversion of Lignocellulosics Pretreated with Liquid Hot Water to Ethanol, (1096).

[21] J.M. Juran, Juran on quality by design : the new steps for planning quality into goods and services, Simon and Schuster, 1992.

[22] S. Adam, D. Suzzi, C. Radeke, J.G. Khinast, An integrated Quality by Design (QbD) approach towards design space definition of a blending unit operation by Discrete Element Method (DEM) simulation, European Journal of Pharmaceutical Sciences. 42 (2011) 106–115. https://doi.org/10.1016/j.ejps.2010.10.013.

[23] A. Hamed, Y. Xia, N. Saha, J. Klinger, D.N. Lanning, J. Dooley, Flowability of Crumbler Rotary Shear Size-Reduced Granular Biomass: An Experiment-Informed Modeling Study on the Angle of Repose, Front Energy Res. 10 (2022). https://doi.org/10.3389/fenrg.2022.859248.

[24] H.M. Beakawi Al-Hashemi, O.S. Baghabra Al-Amoudi, A review on the angle of repose of granular materials, Powder Technol. 330 (2018) 397–417. https://doi.org/10.1016/j.powtec.2018.02.003.

[25] N.S. Cheng, K. Zhao, Difference between static and dynamic angle of repose of uniform sediment grains, International Journal of Sediment Research. 32 (2017) 149–154. https://doi.org/10.1016/j.ijsrc.2016.09.001.

[26] S.B. Savage, K. Hutter, The motion of a finite mass of granular material down a rough incline, J Fluid Mech. 199 (1989) 177–215. https://doi.org/10.1017/S0022112089000340.

[27] G.G.D. Zhou, Q.C. Sun, Three-dimensional numerical study on flow regimes of dry granular flows by DEM, Powder Technol. 239 (2013) 115–127. https://doi.org/10.1016/j.powtec.2013.01.057.

[28] G.I. Tardos, A fluid mechanistic approach to slow, frictional flow of powders, 1997.

[29] R.M. Nedderman, Statics and Kinematics of Granular Materials, Cambridge University Press, 1992. https://doi.org/10.1017/CBO9780511600043.

[30] I. Goldhirsch, Rapid granular flows, Annu Rev Fluid Mech. 35 (2003) 267–293. https://doi.org/10.1146/annurev.fluid.35.101101.161114.

[31] C.S. Campbell, RAPID GRANULAR FLOWS, 1990. www.annualreviews.org.

[32] H. Chen, S. Zhao, X. Zhou, DEM investigation of angle of repose for super-ellipsoidal particles, Particuology. 50 (2020) 53–66. https://doi.org/10.1016/j.partic.2019.05.005.

[33] J. Chen, R. Gao, Y. Liu, Numerical Study of Particle Morphology Effect on the Angle of Repose for Coarse Assemblies Using DEM, Advances in Materials Science and Engineering. 2019 (2019). https://doi.org/10.1155/2019/8095267.

[34] Z.Y. Zhou, R.P. Zou, D. Pinson, A.B. Yu, Angle of repose and stress distribution of sandpiles formed with ellipsoidal particles, Granul Matter. 16 (2014) 695–709. https://doi.org/10.1007/s10035-014-0522-4.

[35] Y. Shimizu, P.A. Cundall, THREE-DIMENSIONAL DEM SIMULATIONS OF BULK HANDLING BY SCREW CONVEYORS, 2001.

[36] D. Kretz, S. Callau-Monje, M. Hitschler, A. Hien, M. Raedle, J. Hesser, Discrete element method (DEM) simulation and validation of a screw feeder system, Powder Technol. 287 (2016) 131–138. https://doi.org/10.1016/j.powtec.2015.09.038.

[37] Q.F. Hou, K.J. Dong, A.B. Yu, DEM study of the flow of cohesive particles in a screw feeder, Powder Technol. 256 (2014) 529–539. https://doi.org/10.1016/j.powtec.2014.01.062.

[38] S. Wang, H. Li, R. Tian, R. Wang, X. Wang, Q. Sun, J. Fan, Numerical simulation of particle flow behavior in a screw conveyor using the discrete element method, Particuology. 43 (2019) 137–148. https://doi.org/10.1016/j.partic.2018.01.016.

[39] L. Pezo, A. Jovanović, M. Pezo, R. Čolović, B. Lončar, Modified screw conveyor-mixers - Discrete element modeling approach, Advanced Powder Technology. 26 (2015) 1391–1399. https://doi.org/10.1016/j.apt.2015.07.016.

[40] D. Minglani, A. Sharma, H. Pandey, R. Dayal, J.B. Joshi, S. Subramaniam, A review of granular flow in screw feeders and conveyors, Powder Technol. 366 (2020) 369–381. https://doi.org/10.1016/j.powtec.2020.02.066.

[41] M. Rackl, W.A. Günthner, Experimental investigation on the influence of different grades of wood chips on screw feeding performance, Biomass Bioenergy. 88 (2016) 106–115. https://doi.org/10.1016/j.biombioe.2016.03.011.

[42] J. Falk, R.J. Berry, M. Broström, S.H. Larsson, Mass flow and variability in screw feeding of biomass powders - Relations to particle and bulk properties, Powder Technol. 276 (2015) 80–88. https://doi.org/10.1016/j.powtec.2015.02.023.

[43] S. Hernandez, T.L. Westover, A.C. Matthews, J.C.B. Ryan, C.L. Williams, Feeding properties and behavior of hammer- and knife-milled pine, Powder Technol. 320 (2017) 191–201. https://doi.org/10.1016/j.powtec.2017.07.002.

[44] J.H. Dooley, D.N. Lanning, C.J. Lanning, Woody biomass size reduction with selective material orientation, Biofuels. 4 (2013) 35–43. https://doi.org/10.4155/bfs.12.72.

[45] M.F. Crowley, H. Sitaraman, J. Klinger, F. Usseglio-Viretta, N.E. Thornburg, N. Brunhart-Lupo, M.B. Pecha, J.H. Dooley, Y. Xia, P.N. Ciesielski, Measurement of Transport Properties of Woody Biomass Feedstock Particles Before and After Pyrolysis by Numerical Analysis of X-Ray Tomographic Reconstructions, Front Energy Res. 10 (2022). https://doi.org/10.3389/fenrg.2022.850630.

[46] P.W. Cleary, M.L. Sawley, DEM modelling of industrial granular flows: 3D case studies and the effect of particle shape on hopper discharge, Appl Math Model. 26 (2002) 89–111. https://doi.org/10.1016/S0307-904X(01)00050-6.

[47] V. Scherer, M. Mönnigmann, M.O. Berner, F. Sudbrock, Coupled DEM–CFD simulation of drying wood chips in a rotary drum – Baffle design and model reduction, Fuel. 184 (2016) 896–904. https://doi.org/10.1016/j.fuel.2016.05.054.

[48] W. Zhong, A. Yu, X. Liu, Z. Tong, H. Zhang, DEM/CFD-DEM Modelling of Non-spherical Particulate Systems: Theoretical Developments and Applications, Powder Technol. 302 (2016) 108–152. https://doi.org/10.1016/j.powtec.2016.07.010.

[49] P.A. Cundall, O.D.L. Strack, A discrete numerical model for granular assemblies, Geotechnique. 29 (1979) 47–65. https://doi.org/10.1680/geot.1979.29.1.47.

[50] M.H. Abbaspour-Fard, Theoretical validation of a multi-sphere, discrete element model suitable for biomaterials handling simulation, Biosyst Eng. 88 (2004) 153–161. https://doi.org/10.1016/j.biosystemseng.2004.03.010.

[51] C.M. Wensrich, A. Katterfeld, Rolling friction as a technique for modelling particle shape in DEM, Powder Technol. 217 (2012) 409–417. https://doi.org/10.1016/j.powtec.2011.10.057.

[52] H. Kruggel-Emden, S. Rickelt, S. Wirtz, V. Scherer, A study on the validity of the multi-sphere Discrete Element Method, Powder Technol. 188 (2008) 153–165. https://doi.org/10.1016/j.powtec.2008.04.037.

[53] Y. Xia, Z. Lai, T. Westover, J. Klinger, H. Huang, Q. Chen, Discrete element modeling of deformable pinewood chips in cyclic loading test, Powder Technol. 345 (2019) 1–14. https://doi.org/10.1016/j.powtec.2018.12.072.

[54] Y. Guo, Q. Chen, Y. Xia, T. Westover, S. Eksioglu, M. Roni, Discrete element modeling of switchgrass particles under compression and rotational shear, Biomass Bioenergy. 141 (2020). https://doi.org/10.1016/j.biombioe.2020.105649.

[55] Y. Guo, Q. Chen, Y. Xia, J. Klinger, V. Thompson, A nonlinear elasto-plastic bond model for the discrete element modeling of woody biomass particles, Powder Technol. 385 (2021) 557–571. https://doi.org/10.1016/j.powtec.2021.03.008.

[56] C.J. Coetzee, Review: Calibration of the discrete element method, Powder Technol. 310 (2017) 104–142. https://doi.org/10.1016/j.powtec.2017.01.015.

[57] D.A. Santos, R. Scatena, C.R. Duarte, M.A.S. Barrozo, Transition phenomenon investigation between different flow regimes in a rotary drum, Brazilian Journal of Chemical Engineering. 33 (2016) 491–501. https://doi.org/10.1590/0104-6632.20160333s20150128.

[58] S.Y. He, J.Q. Gan, D. Pinson, A.B. Yu, Z.Y. Zhou, Flow regimes of cohesionless ellipsoidal particles in a rotating drum, Powder Technol. 354 (2019) 174–187. https://doi.org/10.1016/j.powtec.2019.05.083.

[59] L.F. Orozco, J.-Y. Delenne, P. Sornay, F. Radjai, Rheology and scaling behavior of cascading granular flows in rotating drums, J Rheol (N Y N Y). 64 (2020) 915–931. https://doi.org/10.1122/1.5143023.

[60] H. Hertz, Ueber die Berührung fester elastischer Körper., Journal Für Die Reine Und Angewandte Mathematik (Crelles Journal). 1882 (1882) 156–171. https://doi.org/10.1515/crll.1882.92.156.

[61] R.D. Mindlin, H. Deresiewicz, Elastic Spheres in Contact Under Varying Oblique Forces, J Appl Mech. 20 (1953) 327–344. https://doi.org/10.1115/1.4010702.

[62] J. Ai, J.F. Chen, J.M. Rotter, J.Y. Ooi, Assessment of rolling resistance models in discrete element simulations, Powder Technol. 206 (2011) 269–282. https://doi.org/10.1016/j.powtec.2010.09.030.

[63] A. Stukowski, Visualization and analysis of atomistic simulation data with OVITO–the Open Visualization Tool, Model Simul Mat Sci Eng. 18 (2010) 015012. https://doi.org/10.1088/0965-0393/18/1/015012.

[64] Y. Xia, F. Chen, J.L. Klinger, J.J. Kane, T. Bhattacharjee, R. Seifert, O.O. Ajayi, Q. Chen, Assessment of a tomography-informed polyhedral discrete element modelling approach for complex-shaped granular woody biomass in stress consolidation, Biosyst Eng. 205 (2021) 187–211. https://doi.org/10.1016/j.biosystemseng.2021.03.007.

[65] F. Chen, Y. Xia, J.L. Klinger, Q. Chen, A set of hysteretic nonlinear contact models for DEM: Theory, formulation, and application for lignocellulosic biomass, Powder Technol. (2022) 117100. https://doi.org/10.1016/j.powtec.2021.117100.

[66] Idaho National Laboratory, LIGGGHTS-INL, Https://Github.Com/Idaholab/LIGGGHTS-INL (2021). (n.d.).

[67] C. Kloss, C. Goniva, A. Hager, S. Amberger, S. Pirker, Models, algorithms and validation for opensource DEM and CFD–DEM, Progress in Computational Fluid Dynamics, an International Journal. 12 (2012) 140–152. https://doi.org/10.1504/PCFD.2012.047457.

[68] A.W. Roberts, The influence of granular vortex motion on the volumetric performance of enclosed screw conveyors, 1999.

[69] P.A. Moysey, M.R. Thompson, Modelling the solids inflow and solids conveying of single-screw extruders using the discrete element method, Powder Technol. 153 (2005) 95–107. https://doi.org/10.1016/j.powtec.2005.03.001.

[70] H. Zareiforoush, M.H. Komarizadeh, M.R. Alizadeh, A review on screw conveyors performance evaluation during handling process, Journal of Scientific Review. 2 (2010) 55–66. https://linkinghub.elsevier.com/retrieve/pii/S1537511010000413.

[71] F. Elekes, E.J.R. Parteli, An expression for the angle of repose of dry cohesive granular materials on Earth and in planetary environments, Proc Natl Acad Sci U S A. 118 (2021). https://doi.org/10.1073/pnas.2107965118.

[72] J. Dai, J.R. Grace, Biomass granular screw feeding: An experimental investigation, Biomass Bioenergy. 35 (2011) 942–955. https://doi.org/10.1016/j.biombioe.2010.11.026.

[73] H.J.H. Brouwers, Particle-size distribution and packing fraction of geometric random packings, Phys Rev E Stat Nonlin Soft Matter Phys. 74 (2006). https://doi.org/10.1103/PhysRevE.74.031309.

[74] W.A. Beverloo, H.A. Leniger, J. van de Velde, The flow of granular solids through orifices, Chem Eng Sci. 15 (1961) 260–269. https://doi.org/10.1016/0009-2509(61)85030-6.

[75] S.K. Barik, V.N. Lad, I. Sreedhar, C.M. Patel, Investigation of mass discharge rate, velocity, and segregation behaviour of microcrystalline cellulose powder from a Copley flow tester, Powder Technol. 417 (2023). https://doi.org/10.1016/j.powtec.2023.118234.

[76] J. Mark, N.T. Gray, Annual Review of Fluid Mechanics Particle Segregation in Dense Granular Flows Granular avalanche: a shallow gravity-driven free-surface flow of grains, Annu. Rev. Fluid Mech. 50 (2018) 407–433. https://doi.org/10.1146/annurev-fluid-122316.

[77] D.A. Santos, C.R. Duarte, M.A.S. Barrozo, Segregation phenomenon in a rotary drum: Experimental study and CFD simulation, Powder Technol. 294 (2016) 1–10. https://doi.org/10.1016/j.powtec.2016.02.015.

[78] R. Kumar, A.K. Jana, S.R. Gopireddy, C.M. Patel, Effect of horizontal vibrations on mass flow rate and segregation during hopper discharge: discrete element method approach, Sādhanā. 45 (2020) 1–13. https://doi.org/10.1007/s12046-020-1300-0S.

[79] W. Jin, Y. Lu, F. Chen, A. Hamed, N. Saha, J. Klinger, S. Dai, Q. Chen, Y. Xia, On the Fidelity of Computational Models for the Flow of Milled Loblolly Pine: A Benchmark Study on Continuum-Mechanics Models and Discrete-Particle Models, Front Energy Res. 10 (2022). https://doi.org/10.3389/fenrg.2022.855848.

[80] S.D. Liu, Z.Y. Zhou, R.P. Zou, D. Pinson, A.B. Yu, Flow characteristics and discharge rate of ellipsoidal particles in a flat bottom hopper, Powder Technol. 253 (2014) 70–79. https://doi.org/10.1016/j.powtec.2013.11.001.

[81] S.D. Liu, J.Q. Gan, R.P. Zou, A.B. Yu, Z.Y. Zhou, Wall stress analysis in an unsteady hopper flow with ellipsoidal particles, Powder Technol. 361 (2020) 1–9. https://doi.org/10.1016/j.powtec.2019.11.053.

[82] H. Sun, H. Ma, Y. Zhao, DEM investigation on conveying of non-spherical particles in a screw conveyor, Particuology. 65 (2022) 17–31. https://doi.org/10.1016/j.partic.2021.06.009.

[83] S. Mobarakabadi, E.N. Oskoee, M. Schröter, M. Habibi, Granular transport in a horizontally vibrated sawtooth channel, Phys Rev E Stat Nonlin Soft Matter Phys. 88 (2013). https://doi.org/10.1103/PhysRevE.88.042201.

[84] C.R.K. Windows-Yule, A.D. Rosato, A.R. Thornton, D.J. Parker, Resonance effects on the dynamics of dense granular beds: Achieving optimal energy transfer in vibrated granular systems, New J Phys. 17 (2015). https://doi.org/10.1088/1367-2630/17/2/023015.

[85] H. Cai, G. Miao, Resonant phenomena and mechanism in vibrated granular systems, Phys Rev E. 101 (2020). https://doi.org/10.1103/PhysRevE.101.032902.